Diploma Thesis in Solid State Physics

Vacuum Rabi Splitting at High Drive Powers and Elevated Temperatures

Priska Studer

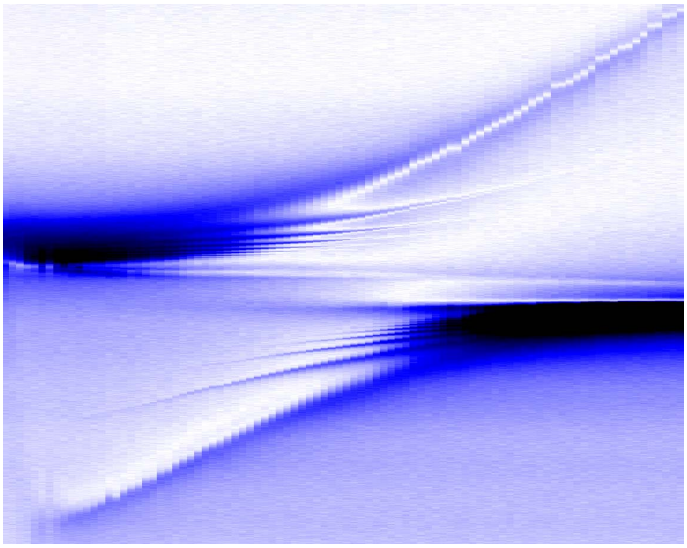

July 2008

supervised by L. S. Bishop, J. M. Chow and Dr. J. Koch
J. M. Fink and Dr. S. Filipp

Quantum Device Lab
of Prof. A. Wallraff
ETH Zurich

in collaboration with the group of Prof. R. J. Schoelkopf and Prof. S. M. Girvin
Yale University

Abstract

Normally, if an atom couples to its electromagnetic environment noise due to vacuum fluctuations will cause the atom to spontaneously decay, emitting a photon which will not interact with the atom again. The strength of interaction between photons and atoms can be increased such that it dominates over dissipative processes by confining the electromagnetic field with a cavity. This is called the strong coupling regime of cavity quantum electrodynamics (QED) [1]. In recent works the strong coupling regime for artificial atoms in quantum dot systems [2] and circuit QED [3] has been reached. This regime can be observed in form of the splitting of the cavity transmission peak into two separated peaks if a resonant atom is placed inside the cavity - an effect called vacuum Rabi splitting.

In this work the vacuum Rabi splitting was measured in circuit QED with increased drive power, which led to two additional features in vacuum the heterodyne tranmission spectrum. A supersplitting of the Rabi peaks into a doublet can be observed and additional peaks with the characteristic $\sqrt{n}$ spacing of the Jaynes-Cunnings ladder appear. The change of shape can be reproduced by describing the qubit and cavity system as an effective two-level system. Additional levels of the qubit and cavity system were included for the detailed theoretical modeling of the measurements. For a consideration of the sample temperature a thermal contact of the cavity and qubit system to a heat bath was assumed, which led to a good agreement between simulation and measurement at elevated temperature up to 140 mK. With another experimental approach where only the electromagnetic signal passing through the cavity is at an increased temperature, a thermometer for the effective cavity and qubit system was successfully realized.

The additional peaks in the vacuum Rabi splitting with increased drive power show a coupling between the quantized microwave field and the anharmonic spectrum of a superconducting qubit acting as an artificial atom. Especially the agreement between simulation and measurement in every peak confirms the validity of the Jaynes-Cummings Hamiltonian for the description of the system and the robustness of circuit QED. By using the vacuum Rabi mode splitting spectrum as a thermometer of the cavity and qubit system, one can test if thermal noise is low enough to prevent thermal population of the cavity. This is necessary to perform experiments in the quantum mechanical ground state.

Cavity QED in superconducting circuits is an excellent tool for investigations in fundamental interaction of light with matter and in quantum information such as multi-level quantum logic.

Contents

Chapter 1

Introduction

The possibility of storing and processing information has influenced society in the last century like never before. With the invention of computers our daily lives have changed. These machines have become ubiquitous fixtures in offices, laboratories and at home, and modern communication possibilities like the internet and cell phones have become indispensable. Furthermore, with new developments of information processing in computers many physical phenomena, like plate tectonic movement and airplane flow resistance, can be modeled and understood.

A classical computer stores information with bits. Bits are realized in a physical system that can either be in the state 0 or 1. With the advent of quantum mechanics a new question arose. What is information in a quantum system that is described by probabilities? In analogy to a classical computer, the smallest piece of information is a quantum bit or qubit. It can be realized from any two quantum states and differs from classical bits in that it can be in the states 0 and 1 simulatneously. This concept of superposition of two states in a quantum system opens many new ways for information technology.
The idea of quantum information processing and quantum computing led to some interesting theoretic results and forecasts. In 1994 Shor developed a quantum algorithm that could factor and take discrete logarithms of large numbers exponentially faster than any known classical algorithm [4]. This has a big impact on cryptography since the RSA public-key systems relies on the fact that numbers are much easier to multiply than to factor [5]. Therefore a quantum computer could successfully attack a RSA system. This led to a big interest in theory and construction of quantum computers. Later, in 1997 Grover was able to show that with a quantum search algorithm the time to search unstructured data can speed up quadratically [6].
Another important application of quantum computers is simulating quantum physics. With a classical computer, even a small quantum system consisting of 300 electron spins is not possible to simulate [7]. The idea arose that with a quantum computer it should be much easier to simulate quantum physics [8]. This would be a revolution in different areas like atomic physics, nano physics and biochemistry and therefore lead to a better understanding of nature.

Since a qubit can be represented by any two distinct quantum states, there are many different possibilities to realize a quantum computer. Ion traps, nuclear and electron spins, photons, and superconducting circuits are some promising realizations of qubits. In order to study

quantum information, a quantum system must be controllable, which means readout by the experimenter and a deterministic coupling between the qubits must be possible. In addition the system must be coherent, and therefore avoid decay and dephasing. These criteria were introduced by DiVincenzo [9]. Coherence can be seen as the presence of interference and is a characteristic difference between a quantum and a classical system. On the other hand, it is also a limiting factor of a quantum computer. Decoherence arises due to noise, meaning the system must be well isolated from noise in the environment while a measurement must be still possible. These requirements seem to be opposed and are therefore very challenging for an experimental realization.

Usually if an atom is coupled to its electromagnetic environment, noise will cause dephasing and lead to decoherence. In cavity quantum electrodynamics (QED), an atom is confined inside a cavity. If the atom decays the emitted photon is reflected many times inside the cavity before it leaks out. This allows the study of the interaction of a single photon with the atom. Confining the photon to a small volume has some other advantages: an increase of the energy density, more chances for the photon to interact with the atom, and a suppression of the spontaneous decay in the dispersive case which leads to longer coherence times.
In circuit QED photons at microwave frequency interact with a qubit that is realized by using Josephson junctions [3]. The circuit is implemented as a macroscopic system on a chip and behaves quantum mechanically like an artificial atom. Compared to atomic realizations of a qubit, this system is very well coupled to other circuits, the parameters can be tuned and therefore it has the advantage of a better data aquisation and manipulation.

In this work we investigate a transmon qubit that is tuned into resonance with the cavity. Since the transmon qubit has a large effective dipole moment [10], a direct measurement of the qubit photon coupling can be done by the vacuum Rabi splitting. This is a fundamental quantum phenomenon because the system can be prepared in a state that is entangled. Entanglement means a symmetric and antisymmetric superposition of states where the individual properties of each state are lost and can be used for teleporting quantum states [11]. The first vacuum Rabi splitting of an intracavity atom was observed by Zhu et. al. [12]. Recent works described vacuum Rabi splitting for artificial atoms in quantum dot systems [2] and circuit QED [3]. Measuring vacuum Rabi splitting in heterodyne transmission with increased drive power leads to two additional features, a supersplitting of the Rabi peaks into a doublet and additional peaks in the resonator transmission spectrum because of transitions to higher energy levels as further investigated in this work.

Chapter 2

Theory

2.1 Cavity Quantum Electrodynamics

Generally, cavity quantum electrodynamics (QED) studies the interaction of atoms with discrete photon modes in a cavity. A model system for light matter coupling is the interaction of a two level system with a cavity via dipole coupling. This can be modeled with the Jaynes-Cummings Hamiltonian

$$H_{JC} = \hbar\omega_r(a^\dagger a + \frac{1}{2}) + \frac{1}{2}\hbar\omega_a\sigma_z + g\hbar(a^\dagger\sigma_- + a\sigma_+) + H_\kappa + H_\gamma, \tag{2.1}$$

where the fist term is the energy of the electromagnetic field, $\langle a^\dagger a\rangle$ counts the number of photons and every photon contributes the energy $\hbar\omega_r$. Even if no photon is inside the cavity, the vacuum field leads to an electromagnetic energy contribution. The second term represents the two-level system where σ_z is a pauli matrix and the level separation is given by $\hbar\omega_a$. Dipole coupling between cavity and two-level system leads to the third term. With $a^\dagger\sigma_-$, $a\sigma_+$ a photon is emitted respectively absorbed from the atom and g is the coupling constant. Finally the losses of the system should be taken into account. H_γ describes the coupling of the atom to other modes than the cavity mode with a decay rate γ of the excited state. H_κ is given due to the fact that the cavity couples to the continuum and therefore photons leak out. The leakage rate is given by $\kappa = \omega_r/Q$, where Q is the quality factor of the cavity. An Illustration of different terms that contribute to the Jaynes-Cummings Hamiltonian is given in Fig. 2.1.

If $g > \kappa, \gamma$ the strong coupling regime is reached where the coherent interaction between cavity and two-level system dominates over the dissipative part. A charactristic signature for the strong coupling regime can be given in the resonant case that enables a free exchange of energy between cavity and qubit. Because of new eigenstates with photon and qubit character (Fig. 2.2) an excitation of the system oscillates between an atomic excitation and a photon in the cavity. This is called a vacuum Rabi oscillation. If many oscillations can be performed before the photon leaks out of the cavity or the atom decays, the strong coupling limit is reached.

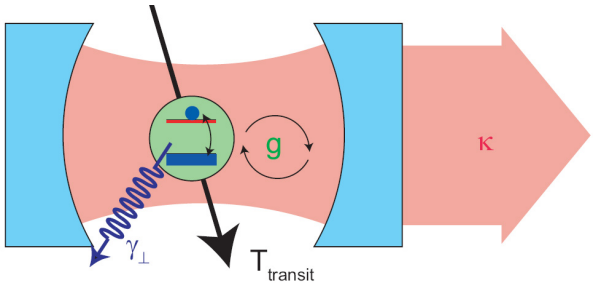

Figure 2.1: Illustration of the different contributions to the Jaynes-Cummings Hamiltonian. A two-level system with decay rate $\gamma_\perp$ traverses the cavity during the time T_{transit}. The two-level system interacts with a single mode of the electromagnetic field with coupling strength g. Loss of photons arises at rate κ. Figure taken from [13].

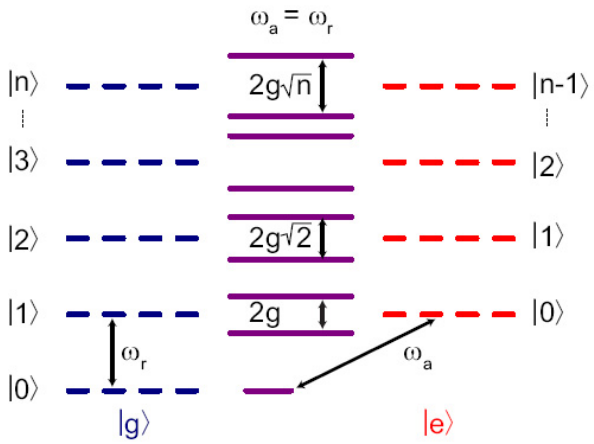

Figure 2.2: Energy level diagram of the Jaynes Cummings Hamiltonian. On the left is the qubit in the ground state $|g\rangle$, on the right in the excited state $|e\rangle$, $|n\rangle$ stands for the photon number. Dashed lines represent an uncoupled system and solid lines represent the dipole coupled states. In the resonant case where $\omega_a - \omega_r = 0$, the coupling leads to new eigentstates. A separation of the energy with $2g\sqrt{n}$ can be observed. Figure taken from [14].

2.2 Cooper Pair Box

There are three different types of qubits based on superconducting circuits, which can be classified according to the three variables charge, flux and phase that are used to control and excite [16]. The qubit type considered here is the Cooper pair box, a charge qubit [17, 18].

The Cooper pair box (CPB) consists of a Josephson junction and a gate capacitance C_g. A Josephson junction is given by two superconducting layers separated by a thin isolator. Even if no external electromagnetic field is applied there can be a super-current across the junction. This is called the Josephson effect. The Josephson junction is described as a circuit element with a Josephson energy E_J and a capacitance C_j. This circuit element allows a coherent tunneling of the Cooper pairs between the two superconducting layers, has an anharmonic spectrum wich is needed to distinguish the different energy levels and low dissipation (Fig. 2.3b).
The part between gate capacitor and isolating layer of the junction is often called the island and the remaining part of the electrode is referred to as the reservoir (Fig. 2.3a). Cooper pairs can be exchanged between island and reservoir. The excess charges on the island are expressed by $n = 2N$, N being the number of Cooper pairs. With an applied voltage V_g the Cooper pairs can be electrostatically induced to tunnel and therefore the reduced gate charge n_g can be changed according to

$$n_g = C_g V_g / e, \tag{2.2}$$

with C_g and V_g being the gate capacitance and the gate voltage respectively.

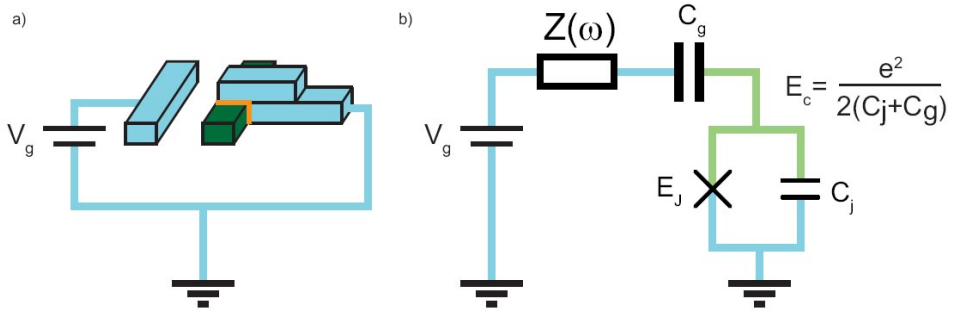

Figure 2.3: (a) A schematical picture of a Cooper pair box. In green we have the island, in orange the isolator and in blue the reservoir. (b) A circuit diagram of the CPB. The island (green) is connected to the reservoir via a Josephson junction which is symbolized by a Josephson element with Josephson energy E_J and a capacitance C_j. With an applied voltage V_g the reduced gate charge n_g can be controlled. The charging energy E_c is given by the total capacitance of the island to ground. Figure taken from [14].

2.2.1 Charge Basis

If $\hat{N}$ is an operator giving the number of Cooper pairs in excess from neutrality in the island, the eigenstates of $\hat{N}$ can be used as a basis for the Hamiltonian. Eigenstates, $|n\rangle$, can be calculated with

$$\hat{N}\,|n\rangle = N\,|n\rangle \qquad\qquad N \in \mathbb{Z}. \tag{2.3}$$

The Hamiltonian for a CPB can be divided into two parts, an electrostatic component and a Josephson component from the Cooper pairs tunneling through the junction.

$$\begin{aligned} H &= H_{el} + H_J \\ &= \sum_{n\in\mathbb{Z}} 4E_c(N - \frac{n_g}{2})^2\,|n\rangle\langle n| - \frac{E_J}{2}\left(|n\rangle\langle n+1| + |n+1\rangle\langle n|\right) \end{aligned} \tag{2.4}$$

$E_C = \frac{e^2}{2C_\Sigma}$ represents the electrostatic energy that is needed to transfer an electron to the island, with $C_\Sigma = C_j + C_g$ being the total capacity of the Cooper pair box. $E_J = \frac{\phi_0 I_c}{2\pi}$ is the Josephson energy, with I_c the critical current over the Josephson junction and $\phi_0 = h/2e$ the flux quantum [19].
The first part of the Hamiltonian leads to parabolas in the energy versus n_g diagram (Fig. 2.4). The parabolas are horizontally shifted with different numbers of Cooper pairs in excess on the island. At a crossing point of two parabolas an energy degeneration of the two charge states occurs. This point is also called a charge degeneracy point. If the exchange of Cooper pairs between island and reservoir is taken into account (coherent tunneling), the charge degeneracy is lifted. An avoided crossing is visible and the eigenstates are a symmetric and an antisymmetric superposition of n and n+1 Cooper pairs on the island, respectively. This leads to two different energy bands, for which the minimal distance is given by E_J. Since the Josephson junction is an anharmonic element the CPB can be used as an effective two level system, a qubit [20].

The charge degeneracy point is an interesting point in terms of charge noise. At this 'sweet spot' [20] the energy of the system is less sensitive to fluctuations of n_g than at other points. This is due to the fact, that the first order contributions are zero at a minimum and therefore the electron dephasing is reduced.

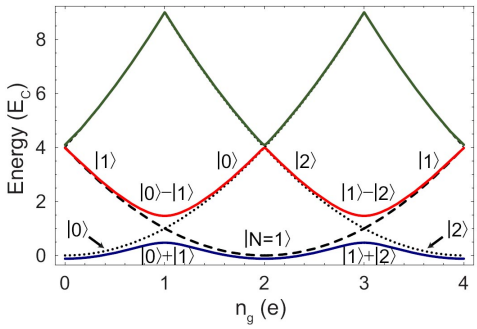

Figure 2.4: Energy levels of a CPB versus gate charge n_g. The dotted and dashed lines represent electrostatic energies for 0,1 and 2 Cooper pairs on the island. Solid lines take in addition the Cooper pair tunneling through the junction into account and are from bottom to top the ground and the first two excited state energy levels with $E_J = E_C$. Figure taken from [14].

2.2.2 Phase Basis

Although the charge basis is very useful to illustrate the states of the CPB, it has a disadvantage. Since the charge basis is unbounded discrete, it is not possible to solve the Hamiltonian in Eq. (2.4) analytically. Phase is the canonical conjugate to charge and in contrast to charge, the superconducting phase difference is continuous and periodic. Therefore the energy levels can be calculated analytically in phase basis.

$$i = [\theta, n] \tag{2.5}$$

With the relation between canonical conjugates, Eq. (2.5), and the periodicity of the phase, the Hamiltonian in Eq. (2.4) can be rewritten in the phase basis.

$$H_{CPB} = 4E_C(i\frac{\partial}{\partial\theta} - n_g/2)^2 \left|\theta\right\rangle \left\langle\theta\right| - \frac{E_J}{2}(e^{i\theta} + e^{-i\theta}) \left|\theta\right\rangle \left\langle\theta\right| \tag{2.6}$$

The time independent Schroedinger equation is $H_{CPB} \left|k\right\rangle = E_k \left|k\right\rangle$. The phase wavefunction $\psi_k = \langle\theta|k\rangle$ and the Schroedinger equation define a differential equation which belongs to the class of Mathieu equations that can be solved analytically [22].

2.2.3 Split Cooper Pair Box

In order to have a second variable to control the energy spectrum of the CPB externally, the idea of a split Cooper pair box was developed [20]. The main difference to the Cooper pair box is the splitting of the junction into two pieces (Fig. 2.5). With this design it is possible to change the Josephson energy E_J with an external flux ϕ through the loop generated by the split junction. The Josephson energy is given by

$$E_J = (E_{J1} + E_{J2})\cos(\pi\frac{\phi}{\phi_0}), \tag{2.7}$$

where E_{J1}, E_{J2} are the Josephson energies of the two junctions. Equation (2.7) is only valid if both Josepohson junctions have the same Josephson energy. Especially for experiments with a transmon qubit, this split design is important because a control of the energy with V_g is not possible. This is further explained in the following section.

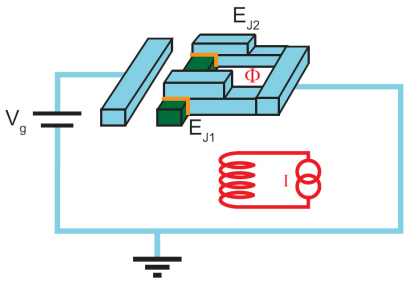

Figure 2.5: Scheme of a split Cooper pair box. The island is connected to the reservoir with two Josephson junctions, each with a Josephson energy E_{J1}, E_{J2}. With an external flux ϕ the Josephson energy E_J can be changed. Figure taken from [14].

2.3 Transmon Qubit

The transmon qubit is a further development of the Cooper pair box and arose from the desire that the qubit is less affected by charge noise. It has a large ratio of Josephson energy to chargeing energy. The main difference to the Cooper pair box is an additional large capacitance between island and reservoir of the two Josephson junctions. This design difference leads to a flatter charge dispersion, a smaller anharmonicity and a stronger coupling to the cavity as further explained in the following sections [10].

2.3.1 Charge Dispersion

A disadvantage of the Cooper pair box is its strong sensitivity to 1/f charge noise. In first order the sensitivity of charge noise can be reduced by operating the qubit at the sweet spot [20]. This point is indicated in Fig. 2.6a with dashed lines. Charge dispersion, $E_m(n_g)$ for the mth energy level, has no slope at the sweet spot and therefore linear contributions have no influence on the qubit. This leads to a drastic improvement of T_2 times [20]. Unfortunately, a changing gate voltage bias is needed to correct the fluctuation of the system that drives it out of the sweet spot regime.
An alternative way to decrease the influence of charge noise is an increase of the ratio E_J/E_C. In Fig. 2.6, a reduction of charge dispersion for increasing E_J/E_C is visible. This leads to the fact that the system gets less influenced by charge noise. Even a complete insensitivity of the eigenenergies to n_g is possible. The total charge dispersion ϵ_m is measured with the peak to peak value for the charge dispersion of the mth energy level

$$\epsilon_m \equiv E_m(n_g = 1/2) - E_m(n_g = 0), \tag{2.8}$$

with E_m being the mth energy level. A more accurate study [10] leads to the following expression for the charge dispersion of the mth energy level:

$$\epsilon_m \cong (-1)^m E_c \frac{2^{4m+5}}{m!} \sqrt{\frac{2}{\pi}} \left(\frac{E_J}{2E_C}\right)^{\frac{m}{2}+\frac{3}{4}} e^{-\sqrt{8E_J/E_C}} \tag{2.9}$$

The strong change of the charge dispersion leads to a promising exponential insensitivity to charge noise as can be seen from Eq. (2.9).

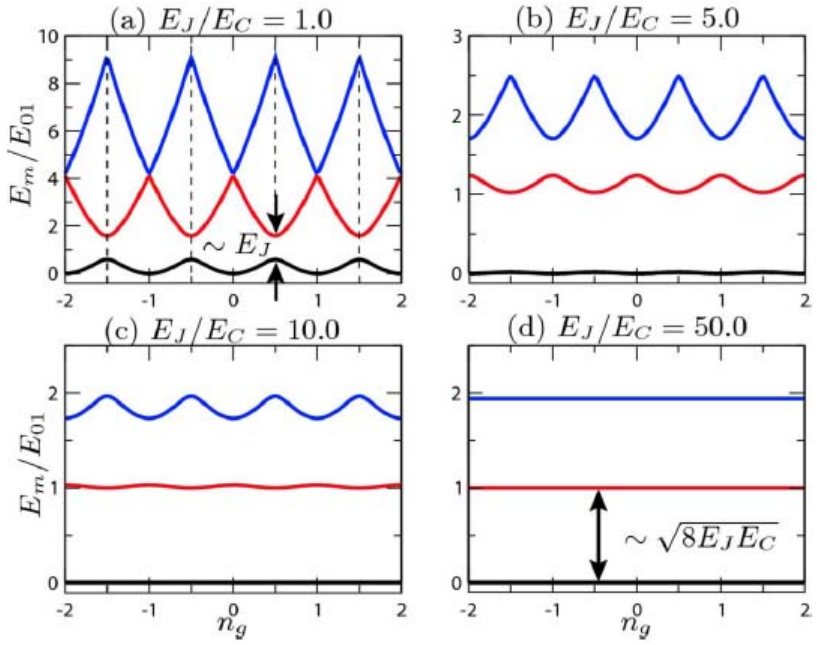

Figure 2.6: Development of charge dispersion with increasing ratio of E_J/E_C. Solid lines represent from bottom to top the ground and the first two excited states energy levels. Energies are given in units of the transition energy E_{01}, evaluated at the degeneracy point $n_g = 1/2$. On the one hand a higher ratio of E_J/E_C flattens the charge dispersion out, on the other hand the anharmonicity decreases. Figure taken from [10].

2.3.2 Anharmonicity

Anharmonicity of the qubit is required to distinguish between the different energy levels and therefore to reduce the many-level system to a two-level system. This is due to the fact that pulses manipulating the qubit transition do not match the frequency to excite the next higher level. The length and shape of the pulse determine its frequency distribution, thus anharmonicity limits the speed for qubit manipulations (Fig. 2.7c). The absolute and relative anharmonicities are given by

$$\alpha \equiv E_{12} - E_{01} \qquad\qquad \alpha_r \equiv \alpha / E_{01}. \tag{2.10}$$

Initially the relative anharmonicity decreases as a function of E_J/E_C and goes through zero. This is called the anharmonicity barrier since at zero anharmonicity all energy levels are equally spaced and it is not possible to use the CPB as a qubit. Finally, with higher E_J/E_C ratio, α_r is negative and increases slowly to zero (Fig. 2.7a).

$$\lim_{E_J/E_C \gg 1} \alpha_r \approx -\sqrt{\frac{E_C}{8E_J}} \qquad\qquad \lim_{E_J/E_C \gg 1} \alpha \approx -E_C \tag{2.11}$$

Since the charge dispersion dicreases exponentially and the anharmonicity only algebraically there is a regime where charge noise is strongly suppressed before α_r equals zero.

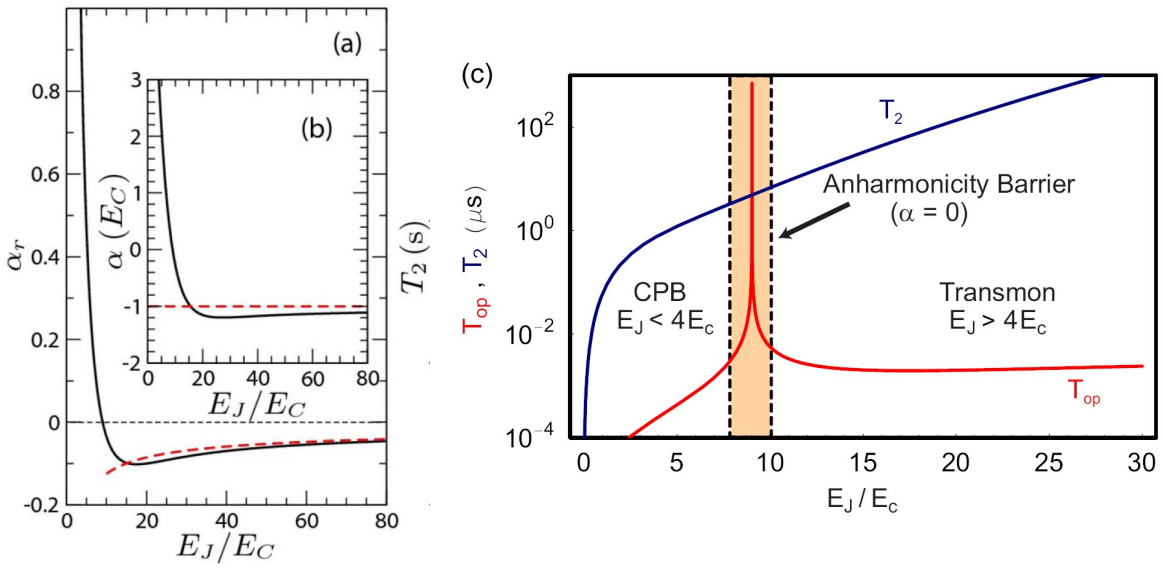

Figure 2.7: (a), (b) Relative and absolute anharmonicity as a function of the ratio E_J/E_C. Figure taken from [10]. (c) Plot of dephasing time T_2 due to charge fluctuations and minimum pulse duration $T_{op} = \frac{1}{\alpha}$ versus E_J/E_C at $n_g = 1$. Minimum pulse duration diverges if the anharmonicity reaches zero (anharmonicity barrier). Figure taken from [14].

2.3.3 Coupling Strength

To reach the strong coupling regime a good coupling of the transmon to the cavity is needed. Although the charge dispersion decreases for a high ratio of E_J/E_C, the coupling between transmon and cavity increases. This is quite remarkable because flattened charge dispersion means that there is no sensitivity to the dc component of n_g while the ac response to the oscillating field even increases [10]. The coupling factors of the cavity field to a transistion between ith and jth level of the transmon are proportional to the charge matrix element

$$g_{ij} \propto \langle i \,|\hat{n}|\, j \rangle \,. \tag{2.12}$$

Asymptotically, the charge matrix elements are given by the following equations [10]:

$$|\langle j+k|\,\hat{n}\,|j\rangle| \overset{E_J/E_C\to\infty}{\longrightarrow} 0, \qquad |k|>1, \tag{2.13}$$

$$|\langle j+1|\,\hat{n}\,|j\rangle| \approx \sqrt{\frac{j+1}{2}}\left(\frac{E_J}{8E_C}\right)^{1/4}. \tag{2.14}$$

Equation (2.13) and (2.14) lead to the fact that only nearest-neighbour coupling $g_{i,i\pm1}$ is relevant in the large E_J/E_C limit. Between neighbouring transmon levels, the coupling strength of the qubit to the cavity even increases with a higher ratio of E_J/E_C. Different coupling factors as a function of E_J/E_C are plotted in Fig. 2.8.

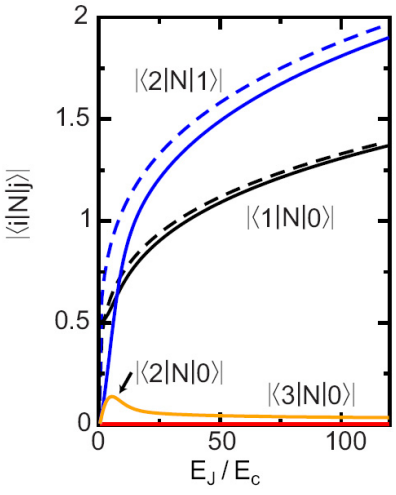

Figure 2.8: Off-diagonal charge matrix elements as a function of E_J/E_C. Solid lines stand for the exact result and dashed lines for the asymptotic behavior that is given in Eq. (2.14). Single level transitions remain large and higher level transitions are strongly suppressed with increasing ratio of E_J/E_C. For coupling at high E_J/E_C only neighboring transmon states are relevant. Figure taken from [14].

2.4 Cavity

In cavity QED, a cavity with a single harmonic mode is needed, which couples to the qubit states. This can be realized with an electrical circuit in the microwave domain [3]. The advantage of a 1D oscillator is its high field density [17]. In addition, a transmission line cavity can be modelled as an infinite series of LCR circuits [23]. On the chip, the transmission line cavity is geometrically realized with a coplanar waveguide design [24, 23].

2.4.1 Transmission Line Resonator

The properties of a transmission line resonator can be modeled with distributed resistors, capacitors and inductors that have a given impedance per unit length (Fig. 2.9). The impedance of an infinitely long lossy transmission line is therefore given by [25]

$$Z_0 = \sqrt{\frac{R^* + i\omega L^*}{G^* + i\omega C^*}}, \tag{2.15}$$

where R^* is the resistance per unit length because of conductor losses, G^* is the shunt conductance per unit length due to dielectric losses between the conductors, L^* is the inductance per unit length given by the total self inductance of the two wires and C^* is the capacitance per unit length between the two conductors.

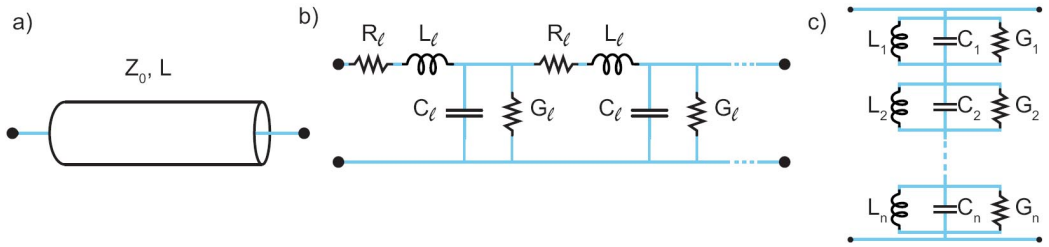

Figure 2.9: a) A transmission line with impedance Z_0 and length L. b) The transmission line can be represented as an infinite series of capacitors and inductors. With the transmission line characteristic impedance Z_0 the capacitance (δC) and inductance (δL) per unit length is determined by $Z_0 = \sqrt{\delta L/\delta C}$. c) This circuit can be transformed into a series of parallel LCR oscillators. Figure taken from [14].

The propagating signal can be specified with a complex propagation constant

$$\gamma = \alpha + i\beta = \sqrt{(R* + i\omega L^*)(G^* + i\omega C^*)}, \tag{2.16}$$

with β describing the phase of the wave and α the attenuation. A transmission line resonator consists of a transmission line with open ends on both sides. Its length l is chosen to be an integer of half a wavelength ($l = n\lambda/2$). Approximating the input impedance around resonance frequency ω_0 and assuming small losses α leads to [25]

$$Z_{in} = \frac{Z_0}{\alpha l + i\pi\frac{\omega-\omega_0}{\omega_0}}. \tag{2.17}$$

The impedance of a parallel LCR oscillator is given by

$$Z_{LCR}(\omega) = \left(\frac{1}{R} + \frac{1}{i\omega L} + i\omega C\right)^{-1}, \tag{2.18}$$

with the resonance frequency $\omega = 1/\sqrt{LC}$ and a quality factor $Q = \omega_0 RC$. The quality factor can also be expressed by the cavity decay rate κ with $Q = \omega_0/(2\pi\kappa)$. Near resonance this equation can be approximated by [25]

$$Z_{LCR}(\omega) = \frac{R}{1 + 2iQ\frac{\omega-\omega_0}{\omega_0}}. \tag{2.19}$$

A comparison of Eq. (2.19) with Eq. (2.17) leads to the idea that the infinite series of capacitors and inductors modeling the transmission line can be mapped on LCR oscillators under following substitutions:

$$R = \frac{Z_0}{\alpha l} \tag{2.20}$$

$$C = \frac{\pi}{2\omega_0 Z_0} \tag{2.21}$$

$$L = \frac{2Z_0}{\pi\omega_0} \tag{2.22}$$

Reference [14] shows a quite close agreement between the LCR model and the transmission line except for the DC behavior. This agreement is even better for higher Q values.

For an interaction with the qubit, the resonator must be connected to the environment. This is realized by means of a capacitive coupling. A connection to the in- and output lines via small capacitors causes a large impedance mismatch and can be thought of mirrors that reflect the photons forth and back. Since the losses are very low, a high quality factor for the cavity can be reached. A detailed description of the capacitive coupling is given in reference [26, 23].

2.4.2 Coplanar Waveguide Resonator

So far the discussion was about microwave cavities independent of their geometrical realization. The transmission line cavity employed is realized in a coplanar waveguide (CPW) design, which is in principle a 2D version of a coaxial cable and has the ground on the same plane as the center conductor. With this geometrical realization the impedance Z_0^{CPW} is determined by the ratio of center conductor width a to gap width s [30]. This has the advantage of a scaling between very narrow gap widths with intense fields where the qubit is placed and a larger gap size for the interface with the printed circuit board. A schematic picture of the coplanar waveguide resonator is shown in Fig. 2.10.
Properties of the coplanar waveguide resonator depend on the exact geometry. The speed of propagation is given by [26, 23]

$$v_{\text{eff}} = \frac{c}{\sqrt{\mu_{\text{eff}}\epsilon_{\text{eff}}}} \approx \frac{c}{\sqrt{\epsilon_{\text{eff}}}}, \tag{2.23}$$

where ϵ_{eff} is the effective dielectric constant and μ_{eff} is the effective magnetic permeability which can be approximated to $\mu_{\text{eff}} \approx 1$ for a non magnetic material. The length l of the

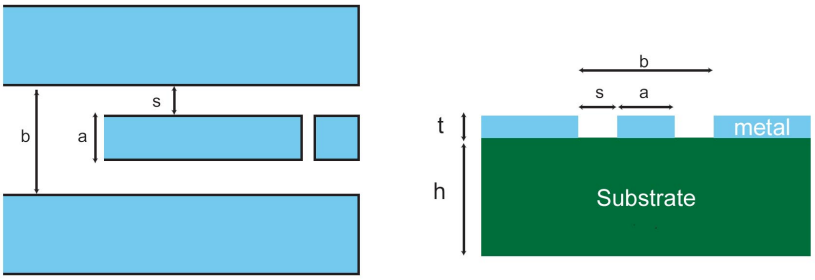

Figure 2.10: Schematic picture of a coplanar waveguide resonator. The length is defined by the two terminating gap capacitors. Figure taken from [14].

coplanar waveguide resonator is determined by the position of the two gap capacitors. This leads to a m-th mode resonance frequency of

$$\omega_0^{CPW} = \frac{\pi m}{l} \frac{c}{\sqrt{\epsilon_{\text{eff}}}}. \tag{2.24}$$

2.5 Coupling of the Qubit to the Cavity

Figure 2.11 shows the arrangement of the cavity and the qubit. The qubit is placed inside the cavity where the first harmonic of the electromagnetic standing wave has the largest amplitude in the electric component. The tunneling of Cooper pairs inside the qubit can be influenced by the center line that acts like a gate electrode for the cooper pair box. Applying a dc voltage to the center line is possible via the input gap capacitor. Another method to control the qubit states is to apply a B-field to tune the flux in the split Cooper pair box.

In addition to the dc voltage there is an ac voltage V arising from photons in the cavity. This voltage can be expressed by $V = Q/C$ where Q is the charge operator. With the resonator frequency $\omega_r = 1/\sqrt{LC}$ the ac voltage can be expressed as

$$V = \sqrt{\frac{\hbar\omega_r}{2C}}(a + a^\dagger) = V_0(a + a^\dagger), \tag{2.25}$$

with V_0 being the rms vacuum fluctuation. In the charge regime the number of excess Cooper pairs can be approximated by $\hat{N} \approx \langle g|\hat{N}|e\rangle\sigma_x$. At $n_g = 1$ this expression can be simplified to $\hat{N} \approx \sigma_x$ leading to the following coupling between the qubit and the cavity,

$$H_{\text{coupling}} = \frac{1}{2}VQ\frac{C_g}{C_\Sigma} = \frac{1}{2}V_0(a + a^\dagger)2e\sigma_x\frac{C_g}{C_\Sigma} = \hbar g(a + a^\dagger)\sigma_x \quad \text{with} \quad g = \frac{e}{\hbar}\frac{C_g}{C_\Sigma}V_0. \tag{2.26}$$

C_g represents the coupling capacitance and C_Σ is the total capacitance of the Cooper pair box. The coupling constant $2\hbar g$ can be interpreted as the energy needed to move a Cooper pair across a portion C_g/C_Σ of the rms vacuum voltage fluctuations V_0 in the resonator.
A rotating wave approximation (RWA) neglects the terms $a^\dagger\sigma_+$ and $a\sigma_-$ can be simplified to

$$H_{\text{coupling}} = \hbar g(a^\dagger\sigma_- + a\sigma_+). \tag{2.27}$$

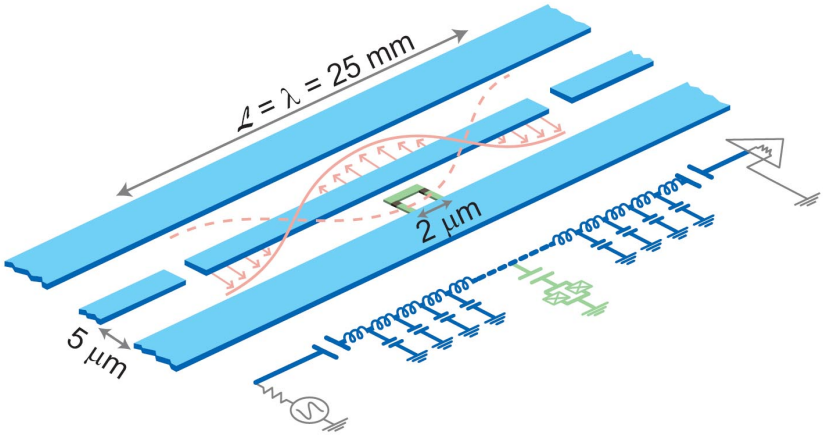

Figure 2.11: Schematic representation of the cavity and the qubit. The Cooper pair box (green) is placed in the center of the cavity (blue). At this point the first harmonic of the electromagnetic standing wave (pink) has an antinode. This configuration leads to a strong dipole interaction between the qubit and the photons. On the bottom is an equivalent lumped element circuit representation. Figure taken from [13].

A RWA is only valid if the energy of the added qubit and photon excitation is much larger than the coupling constant and the difference of the qubit and photon excitation ($\omega_r + \omega_a \gg g, |\omega_r - \omega_a|$). Together with the qubit contribution, the second quantization of the electromagnetic field and the dephasing terms Eq. (2.27) leads to the Jaynes-Cummings Hamiltonian

$$H_{JC} = \hbar\omega_r(a^\dagger a + \frac{1}{2}) + \frac{1}{2}\hbar\omega_a\sigma_z + g\hbar(a^\dagger\sigma_- + a\sigma_+) + H_\kappa + H_\gamma. \tag{2.28}$$

2.6 Hamiltonian of the Driven Cavity QED System

The cavity QED system consists of a transmon inside a cavity and is driven with an RF field at freqency ω_d. To describe this system the Hamiltonian in Eq. (2.28) has to be slightly modified. Since more than two energy levels are taken into account, a general form for H_{transmon} and H_{coupling} is used [13]. In this representation i and j stand for the transmon levels. A driving RF field at ω_d with a drive strength ξ is added [27].

$$\begin{aligned} H_{\text{total}} &= H_{\text{cavity}} + H_{\text{transmon}} + H_{\text{coupling}} + H_{\text{drive}} \\ &= \hbar\omega_c a^\dagger a + \sum_j \hbar\omega_j |j\rangle\langle j| + \hbar\sum_{i,j} g_{i,j}(a + a^\dagger)|i\rangle\langle j| + \hbar\xi(ae^{i\omega_d t} + a^\dagger e^{-i\omega_d t}) \end{aligned} \tag{2.29}$$

In this general form every possible transition between the energy levels is included. A look at Eq. (2.14) tells that at higher ratios of E_J/E_C only neighboring transmon states are relevant for coupling. With this fact H_{coupling} simplifies to a sum over $g_{i,i\pm1}$.

2.6.1 Rotating Wave Approximation and Rotating Frame

Terms in the Hamiltonian that oscillate fast are neglected in the rotating wave approximation (RWA). This assumption is reasonable if the driving frequency ω_d is near resonance with the

qubit because fast oscillating terms will average to zero on any important timescale. Only transitions with the smallest energy difference are considered in a RWA. This leads to the fact that the coupling Hamiltonian stimplifies to two contributions. In the first term a photon is absorbed from the qubit and in the second term the qubit emits a photon.
Unfortunately the Hamiltonian including a driving field is time dependent which complicates the solution of the system. To get rid of the time dependence, a rotating frame at frequency ω_d is considered. Since the frame of reference is time dependent, some additional terms in the Hamiltonian appear. With a rotating wave approximation and in a rotating frame the Hamiltonian changes into the following form [27, 28]

$$H' = \sum_{j=0} \hbar(\omega_j - j\omega_d) |j\rangle \langle j| + \hbar(\omega_r - \omega_d) a^\dagger a + \hbar \sum_{j=0} g_{j,j+1}(a |j+1\rangle \langle j| + a^\dagger |j\rangle \langle j+1|) + \hbar\xi(a + a^\dagger), \tag{2.30}$$

which was used for the numerical simulations in this work.

2.7 Master Equation and Lindblad Operators

On one hand a quantum system (A) should be well protected from the environment (E) to avoid dephasing and on the other hand an interaction is needed to get information about the system's state. In the present case the system consists of cavity and transmon modes. The environment can be thought of as the modes of the field to which the cavity is coupled via transmission or scattering on cavity walls imperfections [31].
Since the environment is complex including a large number of degrees of freedom, it is not possible to calculate every state during the evolution of the A + E system. An analogy to this case is a classical system coupled to a heat bath. In this case a calculation of the movement of every atom is not possible. A description of the system is given by statistical variables like temperature or pressure. A similar approach is taken in quantum mechanics. Quantizing a probability distribution leads to a density matrix. The dynamics of a quantum system A can be described by a differential master equation for the reduced density matrix ρ_A. ρ_A is given by the partial trace of the global density matrix over E. For a reduced density matrix of A the environment E is not needed to be described explicitly.
A linear quantum process $\mathcal{L}_A$, that transforms the density operator into another, can result from the coupling of the system with its environment.

$$\rho_A \rightarrow \mathcal{L}_A(\rho_A), \tag{2.31}$$

with $\mathcal{L}_A$ being a quantum map. Quantum maps can be written in a simple form, called 'Kraus sum representation'.

2.7.1 Kraus Sum Representation

A quantum process has to fulfill a number of criteria to ensure that the resulting density operator is still a positive hermitian operator of trace one with positive eigenvalues, which is required for the probabilistic interpretation of ρ_A. $\mathcal{L}_A$ should be a linear operation preserving hermiticity, conserve positivity and the trace of ρ_A. A further criteria is complete positivity.
Assuming that A has been entangled in the past with a system B, the global system is described by ρ_{AB}. Since B does not interact with A, the superoperator acting on ρ_{AB} is $\mathcal{L}_A \otimes I_B$.

Complete positivity of $\mathcal{L}_A$ means that the complete quantum map must preserve the positivity of ρ_{AB}.

$$\left\langle \phi^{(AB)} \right| \mathcal{L}_A \otimes I_B(\rho_{AB}) \left| \phi^{(AB)} \right\rangle \geq 0, \qquad \forall \quad \left| \phi^{(AB)} \right\rangle \in \mathcal{H}_{AB} \tag{2.32}$$

$\left|\phi^{(AB)}\right\rangle$ represents a state of the $A+B$ System . With these conditions for a quantum map one can show [31] that any $\mathcal{L}_A$ can be written as a finite sum of terms

$$\mathcal{L}_A(\rho_A) = \sum_k E_k \rho_A E_k^\dagger, \qquad \sum_k E_k^\dagger E_k = I. \tag{2.33}$$

E_k are called the Kraus operators and I represents the identity matrix. The goal is to describe the evolution of ρ_A in time. For this purpose the Kraus sum representation gives the dynamic of ρ_A, which is in general not directly helpful because the Kraus operators are time-dependent. This would lead to a generalized master equation [32] that is an integro-differential equation and depends on previous states of the system. With a Markov approximation, wich is further explained in the next section, the evolution of ρ_A can be written in a first order differential master equation with time independent Kraus operators. This assumption can be used by a wide class of physical environments and leads to a fast and easier solution of the Master equation.

2.7.2 Markovian Approximation

Generally a Markov process is a random process whose future probabilities are determined by its most recent values. That means the past or future of the system has no influence on the present state of the system. The environment forgets information about the system after a short time period
In the case of a qubit that is placed into a resonator and interacts with electromagnetic waves, the system can be defined as modes of the cavity and the qubit. A Markov approximation is reasonable in this case since the environment is a large system with many degrees of freedom and it is ideally not affected by its interaction with the cavity and qubit modes. The environment gives no response to the state of the qubit and its cavity modes. Futhermore every electromagnetic wave leaking out of the cavity passes a circulator that is connected to a resistor. Ideally, there is no reflection and therefore the past of the system has no influence on the present state of the qubit and cavity modes.
For a derivation of the Lindblad master equation we look at a small timescale δt and two assumptions are made:

1. $\delta t \ll \tau_S$ (τ_S: characteristic timescale of the system)
2. $\delta t \gg \tau_E$ (τ_E: time over which the environment forgets information about the system)

The second assumption is equal to a Markov approximation. This assumption leads to the fact that the evolution of the system depends only on the present system density matrix. Therefore the density matrix at a time $\delta t + t$ can be written as a Kraus sum representation which depends only on the time t. Under the first assumption we can neglect higher orders of δt since the system density matrix evolves only a little bit in this time interval.

$$\hat{\rho}_S(t+\delta t) = \mathcal{E}(\hat{\rho}_S(t)) = \sum_k \hat{E}_k \hat{\rho}_S(t) \hat{E}_k^\dagger = \hat{\rho}_S(t) + \mathcal{O}(\delta t) \tag{2.34}$$

To match the terminating condition of first order in δt two different types of Kraus operators are needed. Because of the Markov approximation the Kraus operators include no information about previous states of the system and are given by

$$\hat{E}_0 = \hat{I}_S + (\hat{K} - \frac{i}{\hbar}\hat{H})\delta t \qquad\qquad \hat{E}_k = \sqrt{\delta t}\hat{L}_k \qquad k \geq 1, \tag{2.35}$$

with $\hat{H}$, $\hat{K}$ two arbitrary hermitian operators and $\hat{L}_k$ the Lindblad operators that can be either unitary or hermitian. $\hat{I}_S$ represents the identity matrix in the System S.
To fulfill the normalization condition for the Kraus operators a hermitian operator is constricted to a condition given by the Lindblad operators.

$$\sum_k \hat{E}_k \hat{E}_k^\dagger = I_S \qquad \Longrightarrow \qquad \hat{K} = -\frac{1}{2}\sum_k \hat{L}_k \hat{L}_k^\dagger \tag{2.36}$$

Therefore, the dynamic of the system with $\delta t \longrightarrow 0$ is given by the following equation

$$\begin{aligned}
\hat{\rho}_S(t+\delta t) &= [\hat{I}_S + \delta t(\hat{K} - \frac{i}{\hbar}\hat{H})]\hat{\rho}_S(t)[\hat{I}_S + \delta t(\hat{K} + \frac{i}{\hbar}\hat{H})] + \delta t \sum_k \hat{L}_k \hat{\rho}_S(t)\hat{L}_k^\dagger \\
&= \hat{\rho}_S(t) - \left\{ \frac{i}{\hbar}[\hat{H}, \hat{\rho}_S(t)] + \sum_k [\hat{L}_k \hat{\rho}_S(t)\hat{L}_k^\dagger - \frac{1}{2}\left\{\hat{\rho}_S(t), \hat{L}_k^\dagger \hat{L}_k\right\}] \right\} \delta t + \mathcal{O}(\delta t)^2 \\
\frac{d\hat{\rho}_S}{dt} &\overset{\delta t \longrightarrow 0}{=} \frac{1}{i\hbar}[\hat{H}, \hat{\rho}_S(t)] + \sum_k [\hat{L}_k \hat{\rho}_S(t)\hat{L}_k^\dagger - \frac{1}{2}\left\{\hat{\rho}_S(t), \hat{L}_k^\dagger \hat{L}_k\right\}] = \mathcal{L}[\hat{\rho}_S],
\end{aligned} \tag{2.37}$$

where $\mathcal{L}[\hat{\rho}_S]$ is the Lindbladian superoperator for the system. A shorter notation for Eq. (2.37) is given with dissipators $\mathcal{D}[\hat{L}_k]\hat{\rho}_S$.

$$\mathcal{L}[\hat{\rho}_S] = \frac{1}{i\hbar}[\hat{H}, \hat{\rho}_S] + \mathcal{D}[\hat{L}_k]\hat{\rho}_S \tag{2.38}$$

For a closed system only one Kraus operator is considered which leads to the von Neumann equation describing the time evolution of a density matrix in a closed system

$$\partial_t \hat{\rho}_S = \frac{1}{i\hbar}[\hat{H}, \hat{\rho}_S(t)]. \tag{2.39}$$

Looking at a system which is not closed, more Kraus operators are needed for a description and therefore additional terms appear in the von Neumann equation.

In the case of a qubit placed inside the cavity, transverse decay, cavity leakage and pure dephasing should be included with dissipators in the master equation. The simplest version, with the same pure dephasing for every qubit level and a coupling strength $g_{i,j}(E_J/E_C \to \infty)$, Eq. (2.14), is

$$i\hbar\partial_t \rho_S = [H_S, \rho_S] + \kappa\mathcal{D}[a]\rho_S + \gamma_1 \mathcal{D}[\hat{z}]\rho_S + \frac{\gamma_\phi}{2}\mathcal{D}[\hat{q}]\rho_S, \tag{2.40}$$

with $\hat{q} = \sum_j j\,|j\rangle\langle j|$, $\hat{z} = \sum_j g_{j,j+1}\,|j\rangle\langle j+1|$ and $\hat{a}$ being the photon annihilation operator. For our simulation only the steady state is important, for which reason the left side of Eq. (2.40) can be set to zero.

2.7.3 Heat Bath

The previous Lindbladian superoperators were derived for general damping. In this section we consider the specialized case of a reservoir in form of a heat bath at temperature T. The relaxation of the cavity and qubit system in a thermal environment can be obtained from a general thermodynamic argument.
If the system A gains a photon or steps up an energy level in the transmon qubit, the environment E must perform a transition downwards with the same energy difference. This is necessary to conserve the energy of the $A + E$ system. Therefore a given transition in the environment will contribute to the gain of photons or the transition to higher transmon levels at a ratio equal to the probability of finding E in the upper state of this transition divided by the probability of finding it in its lower state. Since we assume that the environment is a heat bath in thermal equilibrium at a certain temperature T, this transition ratio is equal to $e^{-\beta\hbar\omega}$, $\beta = \frac{1}{k_B T}$, according to the Boltzmann distribution. Therefore a prefactor $e^{-\beta\hbar\omega}$ for $\mathcal{D}[a^\dagger]$ and $\mathcal{D}[\hat{z}^\dagger]$ takes account for a finite temperature. For the simulation only one heat bath was assumed which implies that in equilibrium the cavity and qubit system and the heat bath are at the same temperature T.

$$\mathcal{L}[\rho_s] = -\frac{i}{\hbar}[H, \rho_s] + \kappa\mathcal{D}[\hat{a}]\rho_s + e^{-\beta\omega\hbar}\kappa\mathcal{D}[\hat{a}^\dagger]\rho_s + \gamma_1\mathcal{D}[\hat{z}]\rho_s + e^{-\beta\omega\hbar}\gamma_1\mathcal{D}[\hat{z}^\dagger]\rho_s + \frac{\gamma_\phi}{2}\mathcal{D}[\hat{q}]\rho_s \quad (2.41)$$

Assuming an average frequency ω for all transitions, the prefactor $e^{-\beta\hbar\omega}$ allows an estimation of the temperature of the cavity and qubit system.

Chapter 3

Sample Characterization and Fabrication

There are two main components on the experimental sample, the cavity and the transmon qubit. These two components are briefly discussed in the following sections.

3.1 Cavity

For the measured sample in Yale, the cavity frequency is $\omega_r/2\pi = 6.92$ GHz and the quality factor $Q = 23'070$ which implies a cavity linewidth of $\kappa/2\pi = 300$ kHz.
In analogy to mirrors in an optical cavity, gap capacitors reflect the photons back and forth. A high capacitance is realized with fingers in the capacitor gap which increase the area and therefore the capacitance (Fig. 3.1). In order to suppress parasitic modes between top and bottom of the circuit board the top ground plate should be periodically connected to the bottom using vias. Unforunately, there are no vias on the sample used in this work due to the choice of sapphire as substrate material. To avoid parasitic modes, the resonator is confined to a small volume with meanders (Fig. 3.1). This has an additional advantage of placing different cavity sizes on the same circuit board. The cavity frequency and the quality factor can be controlled by the geometry of the resonator. The length of the resonator determines its frequency and the quality factor is given by the size of the coupling capacitors at input and output [24, 23].

The resonator is fabricated using optical lithography. A niobium film is sputtered on top of a sapphire substrate. In a next step a layer of resist is spun on. Afterwards a mask is aligned and the sample is exposed to UV-light which changes the chemical structure of the resist. In the case of a positive resist the exposed part can be removed by a developer. Afterwards the sample is etched via Reactive Ion Etch until the exposed niobium layer is removed. Finally the remaining resist is washed off.
Sapphire is a very hard material, unsoluble in the acids used for ion etching, which leads to better quality resonators because of the smooth substrate surface and low dielectric losses. An advantage of niobium is its high T_c of 9.2 K, which allows a characterization of resonators at liquid helium temperatures (4 K).

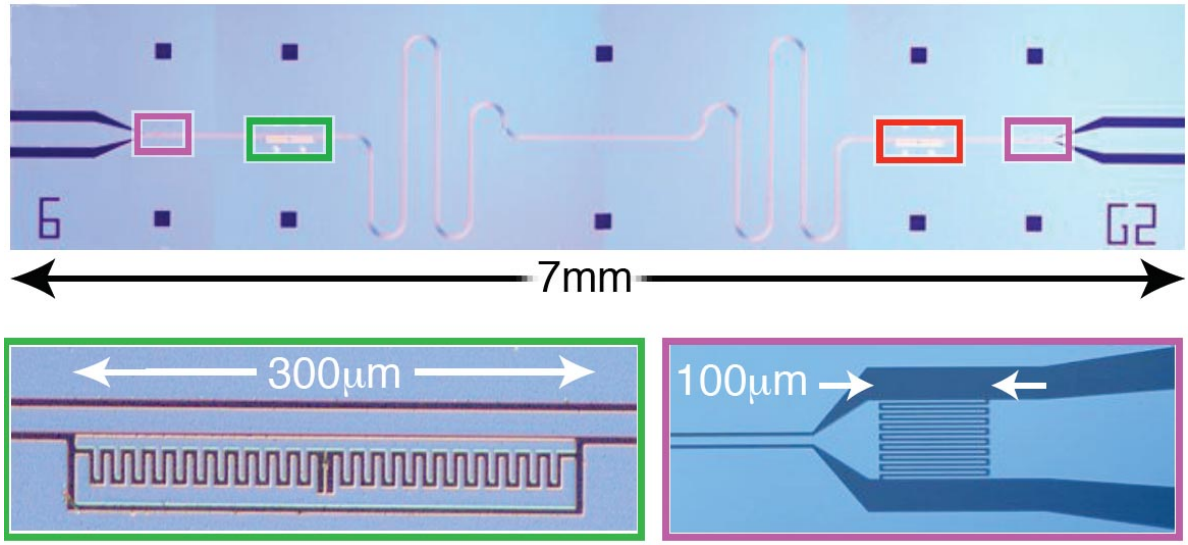

Figure 3.1: Optical image of a sample with two transmons coupled to a microwave cavity, comparable to the sample used in this work. The cavity consists of a coplanar waveguide (light blue) and two coupling capacitors (purple). The two transmon qubits are placed at opposite ends of the cavity, where the electric field has an antinode. In the green inset a transmon is shown; it consists of two superconducting islands that are connected with Josephson junctions and an extra shunt capacitor. Figure taken from [33].

3.2 Transmon Qubit

There are two transmons on the measured sample, each with a different coupling strength to the cavity. The high g transmon is characterized with $g/\pi = 350$ MHz, it has a charging energy of $E_C/h = 400$ MHz and a maximum Josephson energy of $E_J^{\max}/h = 16.2$ GHz. The low g qubit has a coupling of $g/\pi = 94$ MHz, the charging energy is given by $E_C/h = 340$ MHz and the maximum Josephson energy is $E_{J_2}^{\max}/h = 19.86$ GHz. Both transmons have to be placed at antinodes of the electric field in the cavity, as depicted in Fig. 3.1.

The Josephson junction size of 150×150 nm^2 is very small to be reproducibly fabricated by optical lithography. Smaller structures can be produced with e-beam lithography due to the shorter effective wavelength of the electrons compared to UV light. Although aluminum has a lower T_c than niobium, the former is preferred because a directional evaporation is possible and the junction can be produced with the Dolan bridge technique [29]. Aluminum can be thermally evaporated and therefore a lift-off process can be performed. A bilayer resist system is used consisting of PMMA sitting on top of a copolymer. Since the bottom layer is more sensitive to electrons than the top layer, an undercut profile of the resist is obtained. This undercut is big enough to do a liftoff process with aluminum. In order to fabricate a junction, a three dimensional structure of metal, oxide and metal is needed. This is achieved by means of a Dolan bridge technique that uses a bridge of resist to generate a shadow on the substrate. With a double angle deposition it is possible to get the right sequence of aluminum

and aluminum oxide needed for the junction (Fig. 3.2). An advantage of this technique is that it allows making self-aligned small junctions in one step.

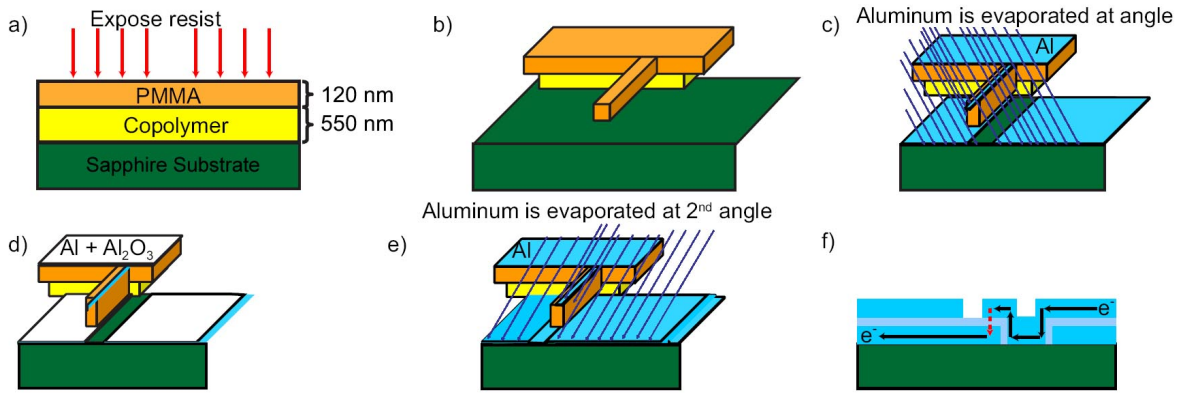

Figure 3.2: Dolan bridge technique. a) A bilayer of resist is exposed to e-beam lithography. b) Because of the different sensitivity of the two resists it is possible to produce a bridge consisting of the top layer. c) The bridge leads to a shadow that causes a gap in the aluminum film. d) A thin film of aluminum oxide is generated when O_2 is let into the evaporation chamber. e) Aluminum is evaporated at a different angle. Because of the shadow under the bridge, there are regions with only a single layer of aluminum. f) A side profile of the structure after the resist is washed off. An electron that goes through the structure must tunnel through the aluminum oxide barrier. Figure taken from [14].

Chapter 4

Measurement Setup

Information about the qubit and cavity state is acquired by probing the sample with microwave radiation and analyzing the signal transmitted through the resonator. The measurement setup consists of four main parts that are described in the following sections. First, a coherent signal has to be generated and modulated at room temperature. Afterwards, the signal enters the fridge and is filtered and attenuated before it interacts with the coupled qubit and cavity system. Finally the transmitted microwaves are amplified, mixed down to lower frequency, filtered and digitally post processed (Fig. 4.2).

4.1 Signal Synthesis

Microwave signal generators from Agilent are used to produce coherent RF signals. In this work only one tone, ω_{RF} is used to probe the cavity and qubit state. For the thermal field measurements in section 6.5 noise is added to the resonator input to simulate thermal noise. The simulation of thermal noise is explained in detail in subsection 6.5.1.

4.2 Cryogenics and Filtering

A Cryoconcept dilution refridgerator or a Kelvinox 400HA dilution fridge from Oxford Instruments is utilized at Yale and ETH respectively to reach a base temperature of 15-20 mK at which the sample is measured. The principle of a dilution fridge is based on cooling via phase change.
When a liquid evaporates a phase change occurs. Molecules require energy to overcome the strong cohesion forces in the liquid to escape into a gas state. If molecules leave the liquid, they take energy from the surrounding environment, thus cooling the liquid since energy is carried away.
Surprisingly a mixture of ^{3}He and ^{4}He separates in two phases at sufficiently low temperature. The concentrated phase consists only of ^{3}He and is lighter than the ^{4}He rich dilute phase. Similarly to a molecule that escapes liquid and cools its surrounding, a ^{3}He atom that moves from the concentrated phase to the dilute phase cools the dilution fridge. In order to reach temperatures of 20 mK, ^{3}He is removed from the fridge with a pump. Because the dilute phase can not have less than 6% ^{3}He at equilibrium, the removed ^{3}He is replaced by ^{3}He from the concentrated phase. This leads to an increased movement of ^{3}He atoms over the phase

boundary and induces further cooling. The dilution fridge has a continuous cycle. The liquid ^{3}He evaporates from the dilute phase in a still and is pumped out of the fridge. Afterwards the gas is purified and recondensed by passing a heat exchanger with liquid ^{4}He. Finally the incoming ^{3}He is precooled with the outcoming ^{3}He liquid by heat exchangers and reenters the ^{3}He rich phase (Fig. 4.1).

In order to operate the system at low temperature of 10-20 mK, noise and heat carried into

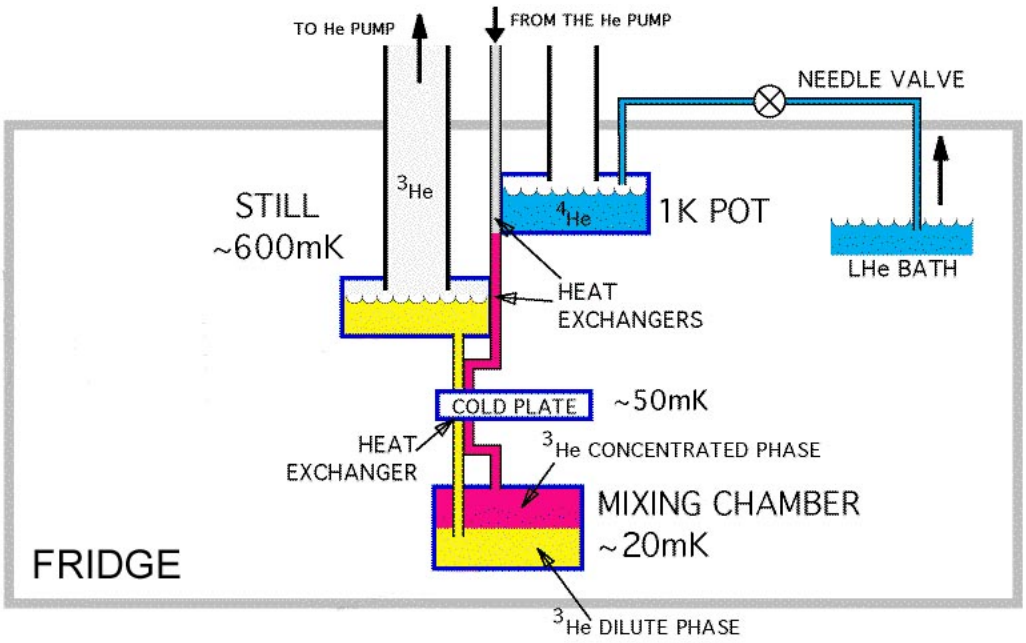

Figure 4.1: Schematic picture of a dilution fridge.

the system by the coaxial cables should be suppressed. The RF drive on the sample is in the order of GHz. In this frequency range Johnson noise is for all temperatures above 100 mK significant. Johnson noise arises due to thermal excitation of the charge carriers in the conductor. A voltage noise power spectral density in this range is proportional to the temperature. Since a large bandwidth is required, the most effective suppression of noise is achieved by attenuating the signal with 30 dBm. For temperatures between liquid He temperature 4 K and base tamperature, the voltage noise power spectral density can be approximated by a radiation spectrum of a one dimensional black body. In order to suppress thermal noise in this section, a second 30 dBm attenuator was installed. Even with a total of 63 dBm attenuation the signal has enough power to perform fast qubit operations in order of ns. An additional effect of the attenuators is that they thermalize the center conducting coaxial cables.

After interacting with the sample the signal is amplified. To avoid unwanted noise emission back into the sample which disturbs the qubit and the desired signal, a circulator is inserted between sample and amplifier. Such a circulator has three ports, one of which is terminated to a 50 Ω resistance. A circulator allows microwave signal propagation in one direction but blocks in the opposite one. The noise generated by the amplifier is dissipated at the 50 Ω termination which is generally thermalized to the cold plate of the fridge. The isolation is about -20 dBm

per circulator.

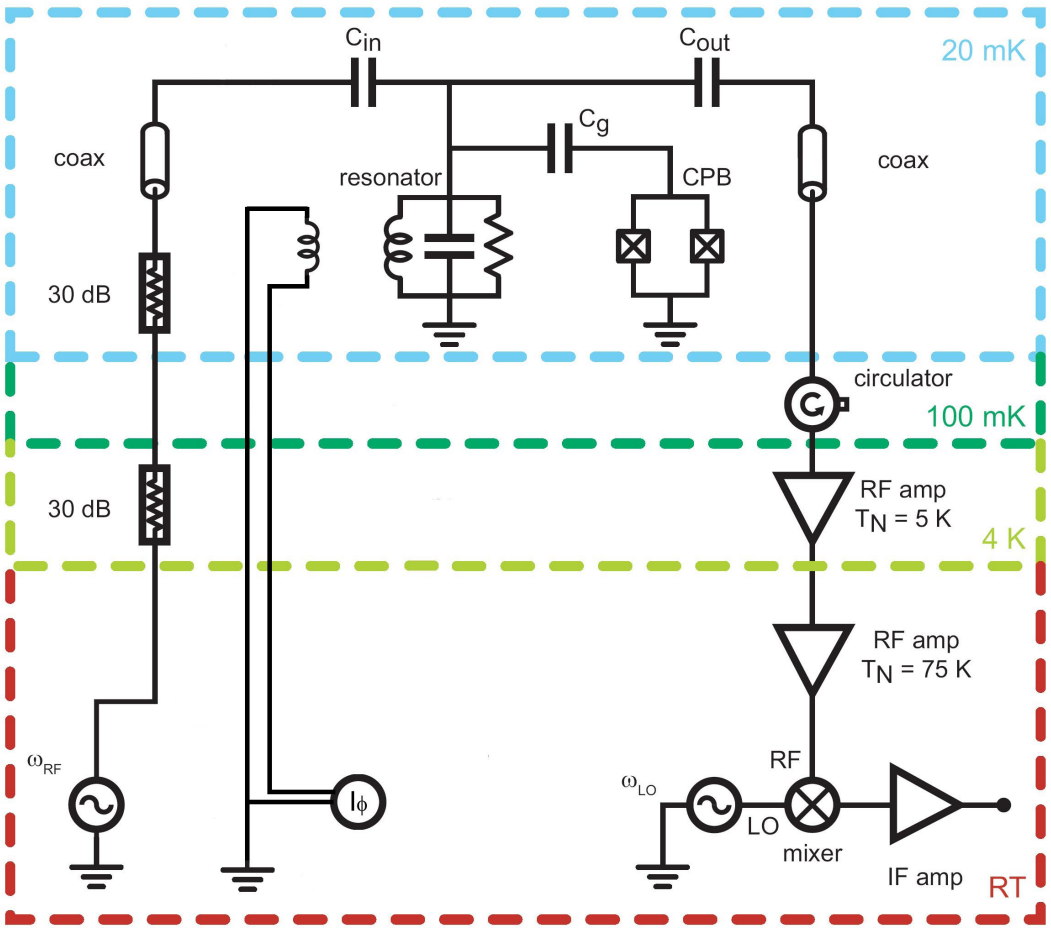

Figure 4.2: Used measurement setup for this work. The coherent input signal ω_{RF} is on bottom left, the output is on bottom right. Colors indicate different temperature stages. The generated signal is filtered, attenuated and heat sunk at different temperature stages before it enters the resonator. After interacting with the qubit, the transmitted signal is amplified, filtered and finally measured. A flux bias line with certain currend I_ϕ and a superconducting coil is scematically represented on bottom left. The different components are further explained in the text.

4.3 Demodulation and Post Processing

The signal is at GHz frequency, ω, and of the form

$$S(t) = A(t)sin(\omega t + \phi(t)), \tag{4.1}$$

with an amplitude $A(t)$ and a phase $\phi(t)$. Computerized data aquisition requires a down conversion from GHz to MHz, which is realized by means of an IQ mixer. The RF port of the mixer is connected to the signal, input two to a local oscillator (LO) with $LO(t) = B(t)sin((\omega + \omega_{if})t)$. The LO signal is split and one branch of the LO signal is phase shifted by $\pi/2$. Then, the RF signal is multiplied with each branch of the LO signal separately. The mixer has an IF bandwith of 500 MHz. Finally, the resulting channels I_{IF} and Q_{IF} are given by

$$I_{IF} = A(t)\cos(\omega_{if}t + \phi(t)); \qquad Q_{IF} = (A(t) + \epsilon_A)\sin(\omega_{if}t + \phi(t) + \epsilon_\phi), \tag{4.2}$$

where ϵ arises due to small inbalances between the two arms of the mixer. Here two different cases are distinguished. If $\omega_{if} = 0$ and only one channel is mixed down this is called homodyne detection. If $\omega_{if} \neq 0$, it is referred as heterodyne. In this work alle measurements are done in heterodyne detection.

For determining the amplitude of the transmitted signal, a single channel digital homodyne method was used. In this method only one channel is considered.

$$IF(t) = A(t)\cos(\omega_{if}t + \phi(t)) \tag{4.3}$$

This signal is digitally multiplied with $\sin(\omega_{if}\tau)$ and $\cos(\omega_{if}\tau)$ seperately and integrated over a time interval $2\pi/\omega_{if}$ to get two phase shifted fourier components of the IF signal,

$$\tilde{I} = \frac{1}{2\pi/\omega_{if}} \int_t^{t+2\pi/\omega_{if}} \cos(\omega_{if}\tau)IF(\tau)d\tau \qquad \tilde{Q} = \frac{1}{2\pi/\omega_{if}} \int_t^{t+2\pi/\omega_{if}} \sin(\omega_{if}\tau)IF(\tau)d\tau. \tag{4.4}$$

From these two fourier components, the amplitude and phase can be reconstructed with

$$\bar{A}(t) = \sqrt{\tilde{I}^2 + \tilde{Q}^2} \qquad \bar{\phi}(t) = \arctan\left(\tilde{Q}/\tilde{I}\right), \tag{4.5}$$

where the bar indicates an average value in a time interval of the size $2\pi/\omega_{if}$. Typically an integration over a time interval of 100 μs is carried out, corresponding to 1000 periods for a typical IF signal of 10 MHz
In order to conduct the measurements in this work the signal frequency is always being changed. In this case, the phase of the signal is arbitraryly set to a new value due to technical reasons. Since only one channel is aquired in these measurements, $\bar{\phi}$ reproduces the phase jumps of the frequency generator and only the amplitude of the signal must be is considered.

4.4 Qubit Control

The qubit frequency $\omega_a \approx \sqrt{8E_J E_C}$ is controlled by applying a perpendicular magnetic field to the squid loop of the qubit, modulating the flux through the split junction. Since the magnetic

flux changes the Josephson energy a control of the qubit frequency is possible.
The magnetic field is generated by passing current through an external superconducting coil. The current bias is applied by using a Yokogawa voltage source across a 10kΩ resistor. The amount of magnetic field produced by the coil is 335 Gauss/A.

Chapter 5

Numerical Calculations

A description of the vacuum Rabi splitting including more than two energy levels is realized with Master equations. The Mathematica program used in this work was written by Lev Bishop and Jens Koch. In this chapter the used parameters and the structure of the program are explained.

5.1 Transmon Calculations

In a first step the eigenvalues and eigenvectors of the qubit Hamiltonian H/E_C (Eq. (2.4)) are calculated in the charge basis by diagonalizing the Hamiltonian. With a cutoff the dimension of the charge basis is restricted. The cutoff is set to 15 therefore the dimension of the charge basis is given by $2 \cdot 15 + 1 = 31$. Eigenvalues of this Hamiltonian correspond to the energies of the transmon levels. From the eigenvectors $\vec{v}_n$ the normalized coupling constants of the transition i→j to the cavity field $g_{i,j}/g_{0,1}$ are calculated.

$$\frac{g_{i,j}}{g_{0,1}} |i\rangle \langle j| = \frac{1}{g_{0,1}} |i\rangle \langle i| \hat{n} |j\rangle \langle j| = (\vec{v}_1, .., \vec{v}_{2p+1}) \begin{pmatrix} -15 & 0 & & \cdots & 0 \\ 0 & -14 & 0 & \cdots & 0 \\ \vdots & & \ddots & & \vdots \\ 0 & \cdots & 0 & 14 & 0 \\ 0 & \cdots & & 0 & 15 \end{pmatrix} (\vec{v}_1, .., \vec{v}_{2p+1})^{\mathsf{T}} \tag{5.1}$$

Now it is possible to calculate the energies and normalized coupling constants of a given n_g and E_J/E_C. The flux dependence of the coupling constants is taken into account with $E_J(\phi)$. Since we want to change the parameters to find a good fit to the measurement, it is convenient to calculate the energies and coupling constants for different parameters and to perform an interpolation afterwards. With this method it is possible to get the energies and coupling constants of new parameters quickly because an interpolation is much faster than the exact numeric calculation.

ω_r	resonator frequency	ω_d	drive frequency
δ	detuning $\omega_r - \omega_{01}$	g	coupling strength g_{01}
ξ	drive strength	γ_ϕ	transmon pure dephasing rate
ejec	E_J/E_C ratio of the transmon qubit	γ_1	transmon energy relaxation rate
κ	cavity relaxation rate		

Table 5.1: Parameters used for calculating the master equation

5.2 Hamiltonian of the System and Solution of the Master Equation

The Hamiltonian of the system is set up in a rotating frame and a rotating wave approximation is considered, Eq. (2.30). Afterwards the Hamiltonian is diagonalized and the energies and eigenvectors are calculated. The environment of the system is taken into account with the master equation (2.40). For setting up the master equation, nine parameters that are listed in table 5.1 are needed.
The drive strength is gnerally given by [35]

$$\xi = \frac{\kappa}{2}\sqrt{\frac{P_{\mathrm{RF}}}{P_{\mathrm{Photon}}}}, \tag{5.2}$$

with $P_{\mathrm{RF}}$the adjusted output power of the signal generator and P_{Photon} the power corresponding to one photon in the cavity. For convenience the drive strength ξ in the simulation is determined by $10^{(n+n_{\mathrm{off}})/20}$, with n being the adjusted output power of the signal generator in dBm and n_{off} a constant offset that represents the attenuation. Finally, the master equation (2.40) is solved in steady state.

The same number of transmon and qubit levels are used for calculating the energies and coupling constants. For the steady state solution of Eq. (2.40) the Hilbert space is constricted to a maximum number of excitations N using the projector $P_N = \sum_{0\leq n+j\leq N} |n,j\rangle\langle n,j|$, with $|n\rangle$, $|j\rangle$ being the cavity and transmon eigenstates respectively. Since $(N!)^2$ dimensional matrices must be inverted for the steady state solution, this is the limiting factor of the program for taking more energy levels into account.

5.3 Fitting Experimental Data

For the solution of the Master equation we get a density matrix ρ_S. The absolute value of the photon annihilation operator expectation value, $|\langle\hat{a}\rangle| = |tr_s(\rho_s\hat{a})|$ can be compared to the measured voltage. This fact is due to the chosen measuring method and is further explained in chapter 6. To get the same amplitude for the simulation and the measurement, there is a linear factor α to be taken into account which describes the scaling between input and output. Even if no qubit is inside the cavity, there is still a small background signal. This is considered with the background parameter b.
For some measurements the background was frequency dependent. A physical explanation for this phenomenon is a second channel between input and output that does not interact with the qubit. The interference of this channel with the signal leads to a frequency dependence of

the background. Therefore the measured amplitude can be calculated with Eq. (5.3).

System parameters are g, κ, ω_r, n, E_J/E_C, γ_ϕ and γ_1. A measurement of these parameters is not always as accurate as needed for the simulations. Especially if the resonator and the transmon qubit are not exactly on resonance, g and E_J/E_C are slightly shifted. To get an optimal agreement between simulation and measurement the system parameters are slightly adjusted. Fit parameters are pt,p_ϕ, n_{off}, α and b.
First the parameters are adjusted by eye to get a good fit to the measurement. Since different parameters can cause the same change in the frequency spectrum if only one input power is conisdered, the data is analyzed for different input powers.

$$V_t = \sqrt{2\alpha \left| tr_s(\rho_s \hat{a}) + 10^{(n+pt)/20} e^{ip_\phi} \right|^2 + b^2} \tag{5.3}$$

n	adjusted power	$\hat{a}$	photon annihilation operator
ρ_s	steady state solution	b	background
α	scalefactor between output and input	pt, p_ϕ	parameters for the 2nd channel

5.4 Optimization

Finding an optimal fit to the measurement by eye valid for different input powers is rather difficult. Therefore an optimization with the Levenberg Marquardt method [34], a nonlinear least square optimization, was used. Since the simulation is limited in the number of photon and qubit levels, some parts of the frequency spectrum can not be fitted well and were therefore excluded from the optimization.

Chapter 6

Results and Discussion

The experiments presented in section 6.1-6.4 are measured at Yale University toghether with Jerry Chow. Experiments in subsection 6.5 were performed at ETH Zurich together with Johannes Fink.

6.1 Vacuum Rabi Splitting at Low Power

To observe vacuum Rabi splitting the qubit is tuned by a magnetic field such that the minimum transition frequency $\omega_a \approx \sqrt{8E_J E_C}$ is resonant with the resonator frequency ω_r. This is only possible with a split junction design, where the Josephson energy E_J depends on the magnetic flux trough the loop generated by the split junction. If degeneracy between cavity and qubit is reached ($\Delta = \omega_a - \omega_r \rightarrow 0$), the eigenstates are not $|e,0\rangle$ and $|g,1\rangle$ any more but even and odd superpositions of these two states $(|e,0\rangle \pm |g,1\rangle)/\sqrt{2}$. To express the superposition of photon and qubit states these eigenstates can be called phobit and quton. If the drive tone is resonant with the transition from the ground state $|g,0\rangle$ to one of the eigenstates with a photonic part, transmission can be observed (Fig. 6.1b).

In Fig. 6.1a the vacuum Rabi avoided crossing is observable. The transmon qubit transition frequency (ω_a) is tuned through the resonator frequency (ω_r) by applying a small magnetic field that modulates the Josephson energy E_J. Transmission of the RF signal at frequency ω_{RF} is represented in colors (blue is high, white is low). A cut through Fig. 6.1a where cavity and qubit are resonant, is given in Fig. 6.2. The minimum separation between the two transmission peaks gives a vacuum Rabi splitting of $2g$=94 MHz. The shape of the two peaks is Lorentzian [3]. If cavity and qubit are slightly detuned from resonance, the two peaks have different amplitudes. The larger peak represents a dressed state which is mostly cavity like and the smaller peak represents a state which is mostly qubit like with only a little bit of photon character. Far away from the avoided crossing the states are either qubit or single photon excitation and therefore only the photon state is observable in a resonator measurement.

6.2 Shape of the Rabi Peak at High RF Power

In the previous section a vacuum Rabi splitting at a power of -23 dBm was observed. For an investigation of the vacuum Rabi splitting at high RF power we look first at one Rabi peak.

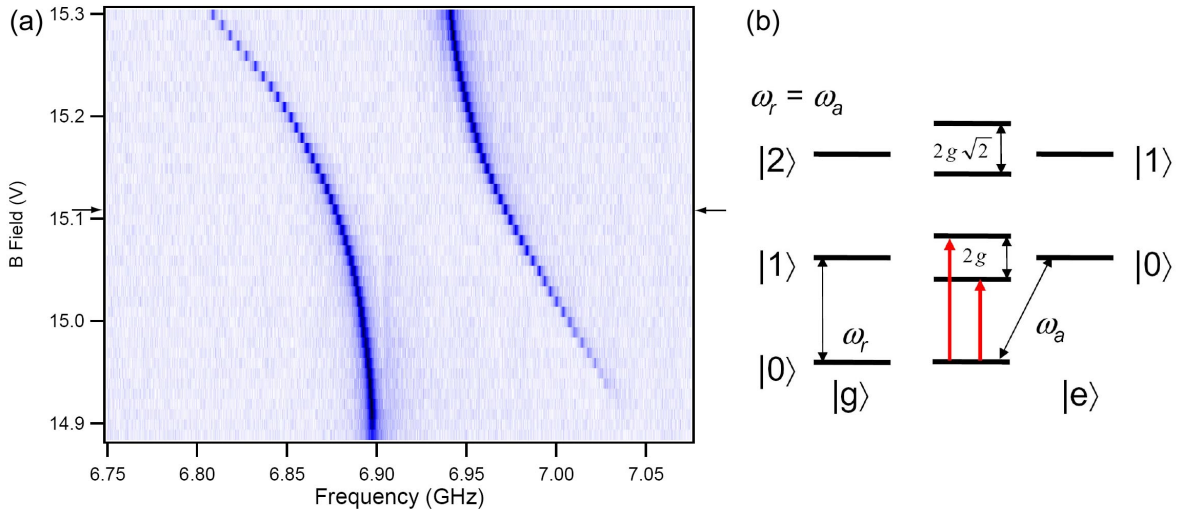

Figure 6.1: (a) Vacuum Rabi avoided crossing. A magnetic field modulates the Josephson energy and therefore the transmon frequency ω_a. Colors reperesent the transmission amplitude of the RF signal (blue is high, white is low) (b) Energy level diagram. Transitions leading to the vacuum Rabi peaks are indicated with red arrows.

In figure 6.3a the Rabi peak development with increasing RF power is visible. Colors indicate the transmission amplitude of the RF signal at frequency ω_{RF} (blue is high, white is low). The peak changes its Lorentzian shape with increasing power and begins to broaden. At a RF power of -21 dBm an additional effect is visible, a dip in the middle of the peak occurs. This dip increases with higher RF power until the Rabi peak is entirely separated into two peaks. For a better visibility cuts through the density plot are given in Fig. 6.3b on the right hand side. From bottom to top the RF power is increased and an asymmetric supersplitting can be observed.

There are two different explanations for the dip in the Rabi peak at high power. An intuitive physical understanding can be achieved with an analysis of the effective Hamiltonian. For a more exact and more analytical explanation the Bloch equations are used. These two cases will be explained in the next sections.

6.2.1 Effective Two-level System

For a system with $g \gg \kappa, \gamma$ the transitions leading to the Rabi peaks are well separated in the energy diagram (Fig. 6.4a). Therefore the ground state $|0, g\rangle$ and the asymmetric combination of the first level $\frac{1}{\sqrt{2}}(|0, e\rangle - |1, g\rangle)$ can be considered as an effective two level system (Fig. 6.4b),

$$\left|\tilde{\uparrow}\right\rangle = \frac{1}{\sqrt{2}}\left(|1, g\rangle - |0, e\rangle\right) \qquad \left|\tilde{\downarrow}\right\rangle = |0, g\rangle\,. \tag{6.1}$$

All experiments are measured in transmission. According to input and output theory [37] a signal of $b_{out} = \sqrt{\kappa}a$ is measured. Since the measurement is in heterodyne mode and only the

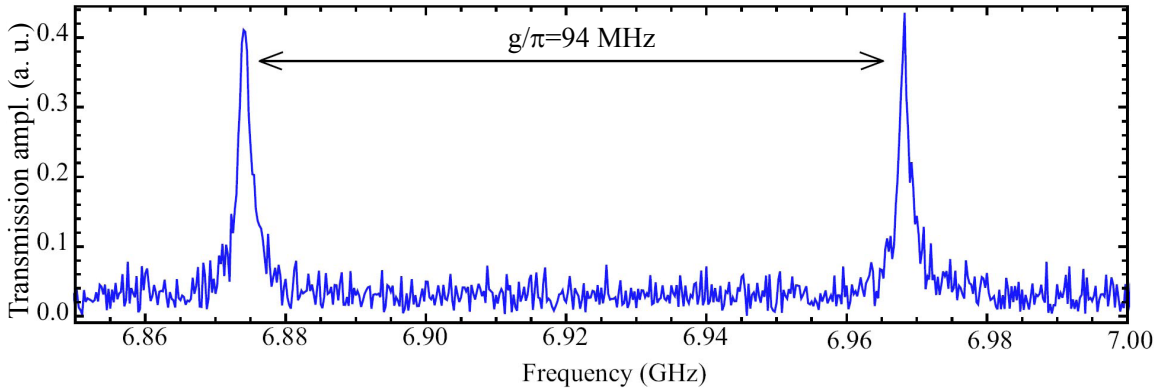

Figure 6.2: Cut through the density plot in Fig. 6.1(indicated with arrows). A vacuum Rabi splitting of g/π=94 MHz is observed.

amplitude A is measured, the signal is proportional to $|\langle a\rangle|$.

$$I = \left\langle b_{out} + b_{out}^{\dagger} \right\rangle \qquad Q = \left\langle i b_{out} - i b_{out}^{\dagger} \right\rangle$$
$$A = \sqrt{I^2 + Q^2} = 2\,|\langle b\rangle| = 2\sqrt{\kappa}\,|\langle a\rangle| \tag{6.2}$$

To understand the measurement it is important to know how the photon annihilation operator $\hat{a}$ changes the effective two-level system.

$$a\left|\tilde{\downarrow}\right\rangle = 0 \qquad a\left|\tilde{\uparrow}\right\rangle = \frac{1}{\sqrt{2}}\left|\tilde{\uparrow}\right\rangle \Rightarrow a \rightarrow \tilde{\sigma}^{-} \tag{6.3}$$

Since the operator a changes pseudo spin up to spin down, it can be interpreted as a lowering operator $\tilde{\sigma}^{-}$ for the effective two level system. For a description of the dynamics, the driven Jaynes-Cummings Hamiltonian for a two level system in RWA and rotating frame (cf. Eq. (2.30)) is needed.

$$H = \frac{1}{2}\hbar(\omega_a - \omega_d)\sigma_z + \hbar(\omega_r - \omega_d)a^{\dagger}a - \hbar g(a^{\dagger}\sigma^{-} + a\sigma^{+}) + \epsilon(a + a^{\dagger}) \tag{6.4}$$

At resonance ($\omega_r = \omega_a$) we introduce a detuning $\Delta = \hbar(\omega_r - \omega_d) = \hbar(\omega_a - \omega_d)$ for convinience. Because only the effective two level system with its pseudo spin states is considered, a projection $P = \left|\tilde{\downarrow}\right\rangle\left\langle\tilde{\downarrow}\right| + \left|\tilde{\uparrow}\right\rangle\left\langle\tilde{\uparrow}\right|$ to this hilbertspace is needed. This leads to an effective Hamiltonian

$$H_{\text{eff}} = \frac{\Delta - \hbar g}{2}\tilde{\sigma}_z + \frac{\epsilon}{\sqrt{2}}\tilde{\sigma}_x = \Delta'\tilde{\sigma}_z + \Omega\tilde{\sigma}_x. \tag{6.5}$$

For a pseudo spin system H_{eff} characterizes two magnetic fields, one in x direction and one in z direction. The pseudo spin precesses around the effective magnetic field B_{eff}, as depicted in Fig. 6.5a.

At high power is $\Omega \gg 1$ and the pseudo spin precesses a long time around B_{eff}, before it relaxes back to the ground state. Decoherence leads to a phase change of the spin. On average

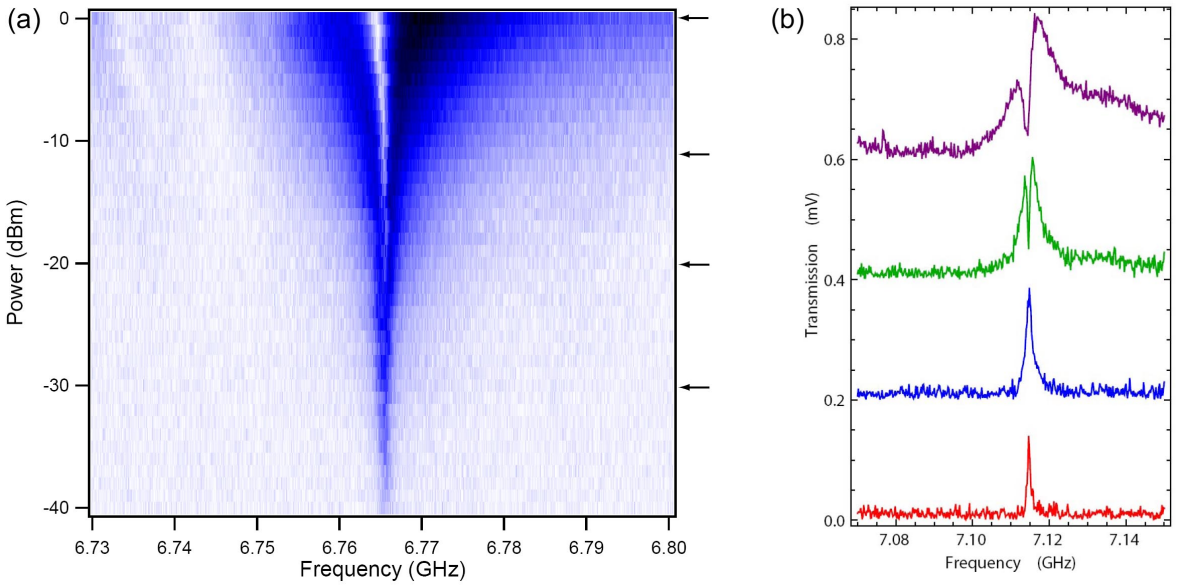

Figure 6.3: (a) Transmission (blue is high, white is low) as a function of frequency and RF power is visible. With higher RF power the transmission peak of the vacuum Rabi splitting is broadened and shows a dip in the middle. (b) Cuts through the density plot (indicated with arrows) with higher RF power from bottom to top, displaying a development from a Lorentzian peak to an asymmetric doublet. The offset between the cuts is for a better visibility.

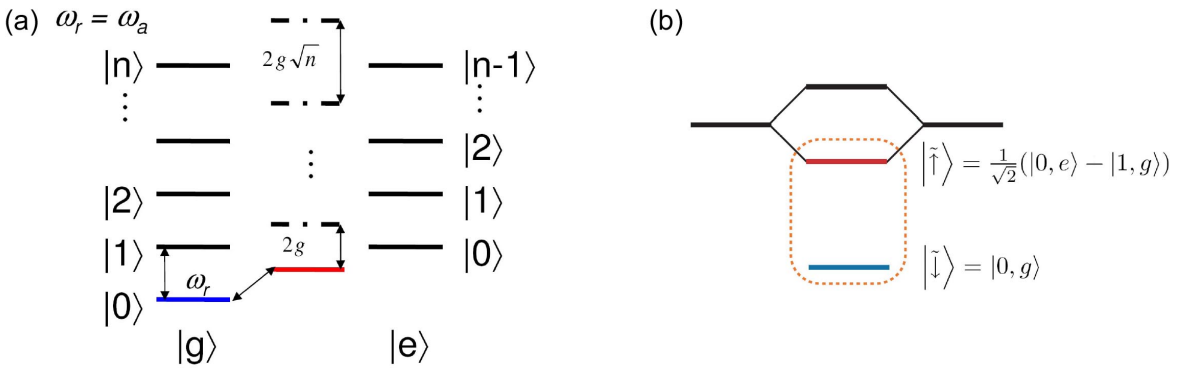

Figure 6.4: (a) Since $g \gg \kappa, \gamma$, the two energy levels leading to the Rabi peaks are well separated. Therefore the ground state $|0,g\rangle$ and the asymmetric combination $\frac{1}{\sqrt{2}}(|0,e\rangle - |1,g\rangle)$ can be considered as an effective two level system. (b) The effective two level system with pseudo spin up $\left|\tilde{\uparrow}\right\rangle$ and spin down $\left|\tilde{\downarrow}\right\rangle$ is indicated with a dashed line.

the state of the system is in the middle of the precession circle around B_{eff}, which is indicated in Fig. 6.5*a* with a green arrow. It was shown that the measurement signal is proportional to $|\langle\tilde{\sigma}^-\rangle|$. Since $\sigma^- = \sigma_x + i\sigma_y$ and B_{eff} has no contribution in y direction, the projection onto the x-axis leads to the measured signal. This projection is given with a green arrow in Fig. 6.5 and can be expressed in terms of Ω and Δ' with

$$T = \frac{\Delta'\Omega}{\Delta'^2 + \Omega^2}. \tag{6.6}$$

The absolute value of the projection as a function of the detuning is shown in Fig. 6.5b. With this graphic picture a splitting of the Lorentzian peak can be understood.

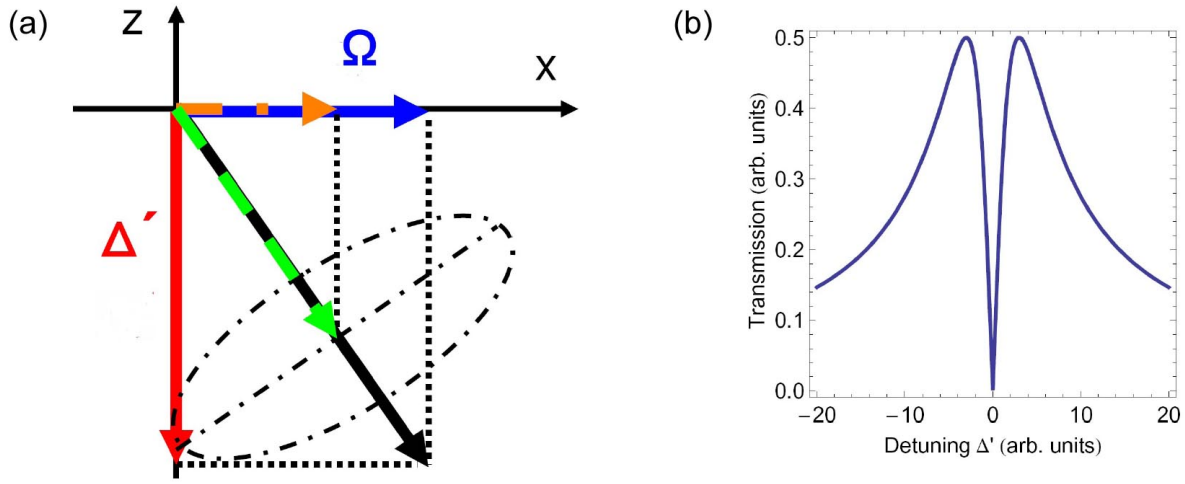

Figure 6.5: (a) A graphic representation of the effective Hamiltonian for the speudo spin. The pseudo spin rotates around an effective magnetic field with a z-component $-\Delta'$ and a x-component Ω. On average, the state of the system is given by the dashed green arrow and the measured component is its projection on the x-axis indicated with a dashed yellow arrow. This leads to a reduced transmission at zero detuning. (b) Transmission from Eq. (6.6) plotted as a function of detuning Δ'.

At low power Ω is much smaller and the precession of the pseudo spin is slower. Therefore the spin does not complete a whole circle around B_{eff}, the system is on average near the ground state and no splitting occurs. A more analytical explanation for the splitting of a Rabi peak at higher power is given by Bloch equations.

6.2.2 Bloch Equations

The dynamic of the pseudo spin under influence of two magnetic fields Δ' and Ω can be described with Bloch equations. For this purpose the pseudo spin is written as a polarization

vector on the Bloch sphere $\vec{P} = (x, y, z)$, $P_i = |\langle \sigma_i \rangle|$ and a rotating frame of reference is chosen.

$$\begin{aligned} \dot{x} &= -\frac{x}{\tilde{T}_2} - \Delta' \\ \dot{y} &= \Delta' x - \frac{y}{\tilde{T}_2} - \Omega z \\ \dot{z} &= \Omega y - \frac{1}{\tilde{T}_1}(z - \bar{z}) \end{aligned} \tag{6.7}$$

$\tilde{T}_1$ represents the relaxation time and $\tilde{T}_2$ the dephasing time of the effective two-level system. At zero temperature $\bar{z} = -1$ and for the characteristic timescales exists the relation

$$\tilde{T}_1^{-1} = 2\tilde{T}_2^{-1} = \frac{1}{2}(T^{-1} + \kappa). \tag{6.8}$$

Since we are only interested in the steady state the left side of the Bloch equations can be set to zero. The measured component is given by

$$\left|\langle \tilde{\sigma}^- \rangle\right| = \frac{\Omega\sqrt{\Delta'^2 + \tilde{T}_2^{-2}}}{\tilde{T}_2^2\Delta'^2 + \tilde{T}_1\tilde{T}_2\Omega^2 + 1} \tag{6.9}$$

and describes the transformation of a Lorentzian peak to a split peak at higher power.

6.2.3 Simulations Including Higher Energy Levels

The consideration of an effective two-level system with the Bloch equations leads to a dip in the middle of the Rabi peak. A plot of transmission as a function of detuning is given in Fig. 6.5 on the right side. In contrast to the measurement, this plot shows two peaks that have the same amplitude. In order to describe the asymmetry of the doublet, higher energy levels have to be taken into account. Cuts through the density plot in Fig. 6.3 at four different powers are shown in Fig. 6.6. The black lines are simulations based on the master equation given in Eq. (2.40). A maximum number of seven excitations is taken into account, wich means $n + j \leq 7$ with $|n\rangle$, $|j\rangle$ being the cavity eigenstates and the qubit eigenstates respectively. An optimization of the paramters was done with a nonlinear least square method taking all RF powers into account. By including a maximum number of seven excitations a good agreement between simulation and measurement is obtained.

6.3 Vacuum Rabi Splitting at High Drive Power

In the previous section the shape of a Rabi peak with increasing RF power was described. The occupation of higher energy levels leads, in addition to the dip in the Rabi peak, to other new structures in the transmission spectrum at high RF power. In order to observe the influence of high RF power on the resonator transmission in the frequency range between the Rabi peaks the qubit with a low coupling constant was measured at different RF powers (Fig. 6.7a). Transmission of the RF signal at frequency ω_{RF} is given in colors (blue is high, white is low). For a power of -8 dBm two new peaks appear at 6.88 GHz and 6.95 GHz (indicated with dashed arrows). These are two photon transitions from the ground state to the second excited state.

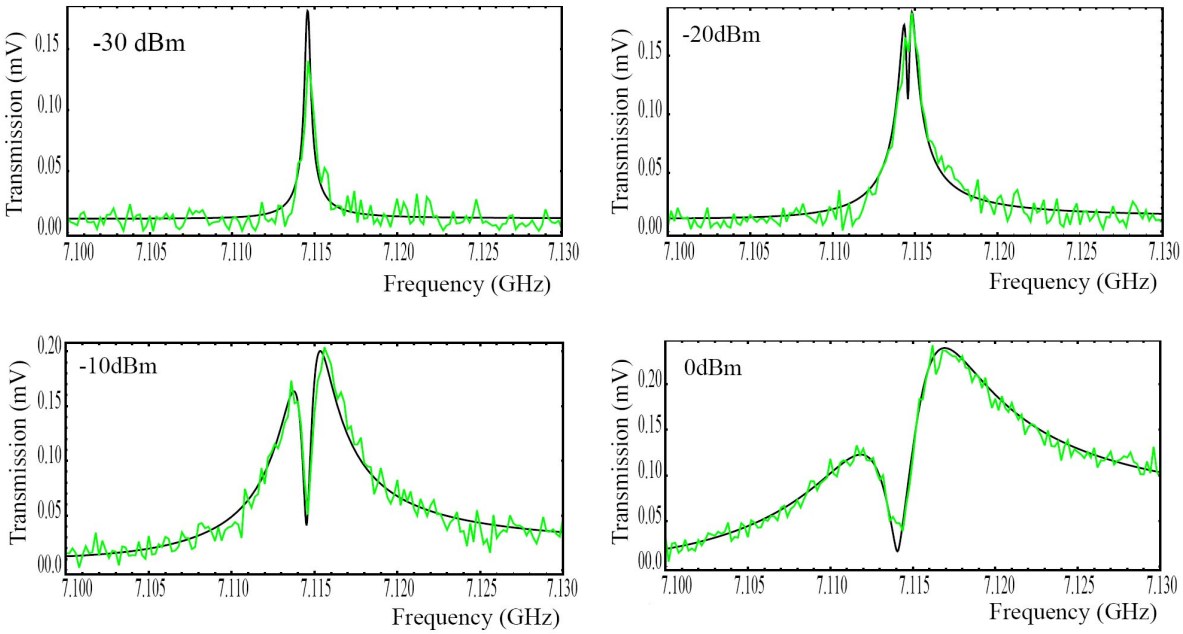

Figure 6.6: Cuts through the density plot in Fig. 6.3 at four different RF powers. The black lines are simulations based on a master equation that includes a maximum number of seven excitations. A good agrement between simulation is obtained, especially for the asymmetric doublet at high drive power.

In Fig. 6.7b the transitions causing the new peaks are indicated in the energy diagram with dashed lines.

Cuts through the density plot (Fig. 6.7a) at different RF powers are shown in Fig. 6.8. The simulation (in black) is based on the Lindbladian superoperator in Eq. (2.40) with a maximum number of seven excitations. A good agreement with the measurement is reached even for the two photon transitions at -3 dBm and -8 dBm. Between 6.9 GHz and 6.95 GHz additional peaks are visible due to thermal excitation of the sample.

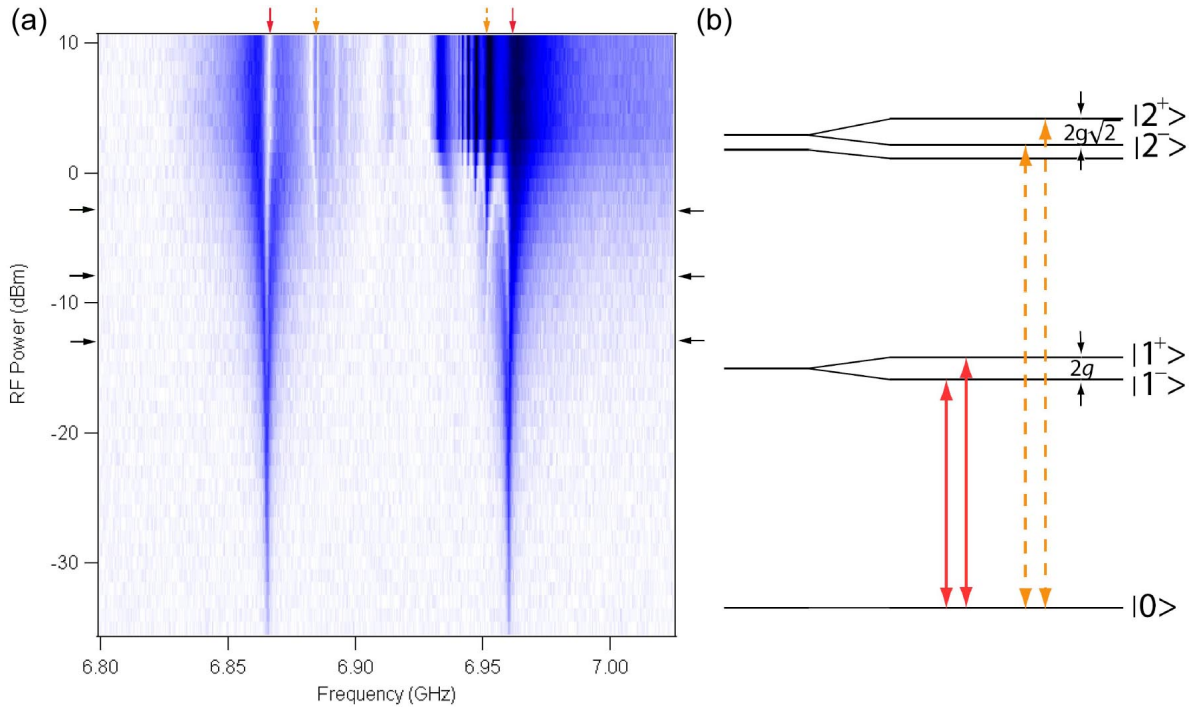

Figure 6.7: (a) Transmission (blue is high, white is low) as a function of frequency ω_{RF} and RF power. Additional peaks are visible at -8 dBm arising due to excitations of the system to higher energy levels. (b) Energy diagram including a maximum of two excitations. Transitions leading to the vacuum Rabi peaks are indicated with solid arrows. Two photon transitions are depicted with dashed arrows.

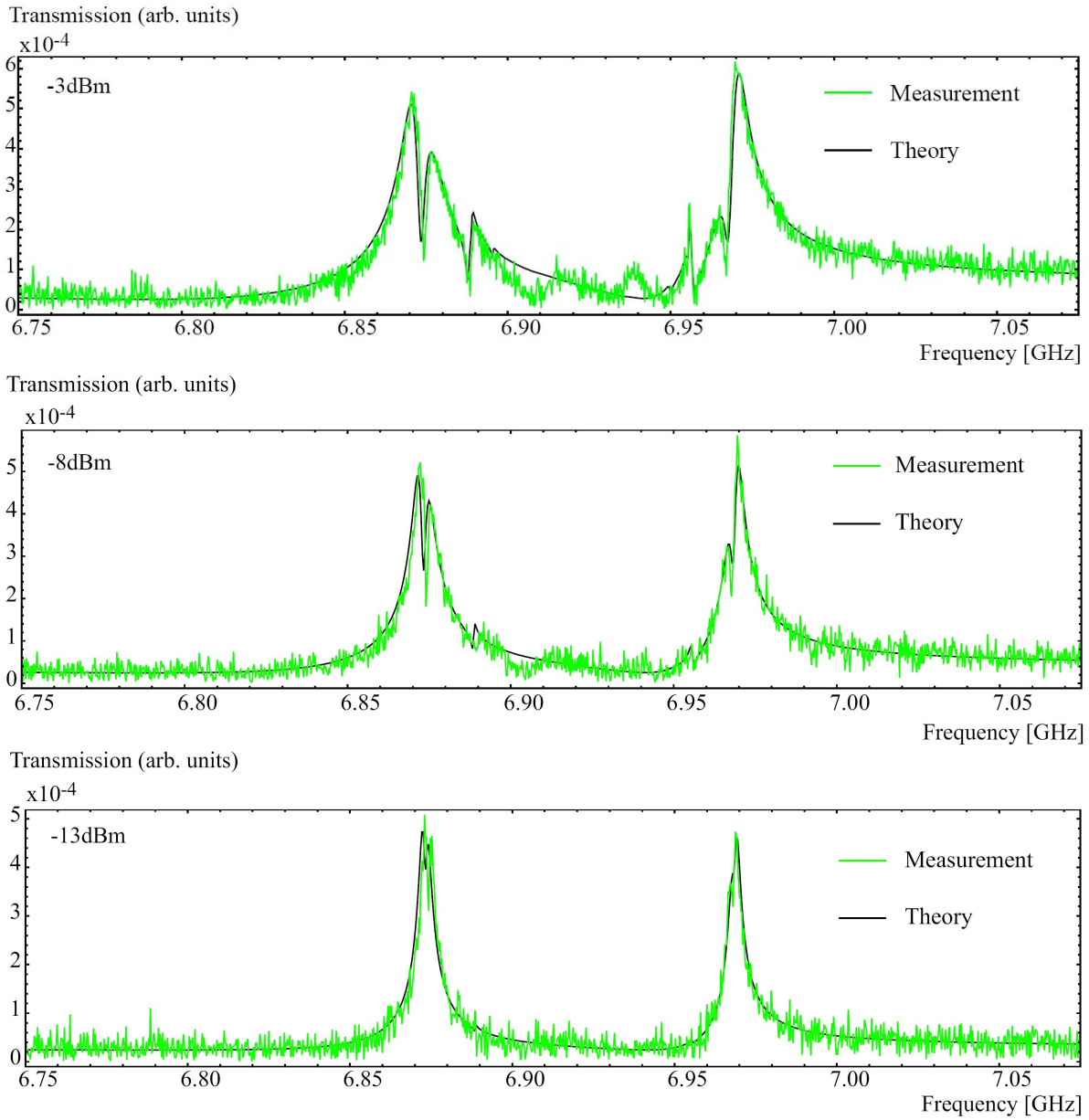

Figure 6.8: Cuts through the density plot in Fig. 6.7a at three different RF powers (indicated with arrows). The simulations which take a maximum number of seven excitation into account are in good agreement with the measurements. For -3 dBm additional peaks between the two Rabi peaks are visible that do not match with the theory. These peaks arise due to thermal excitation.

6.3.1 Avoided Crossing at High Drive Power

Fig. 6.9 shows an avoided crossing at a drive power of 4 dBm. In addition to the avoided crossing at low drive powers [3], fan-like structures due to multiphoton transitions are visible. Every individual branch can be identified with a transition in the Jaynes-Cummings ladder. Each multiphoton tranistion appears initially as a single peak and supersplits as the drive power is increased.

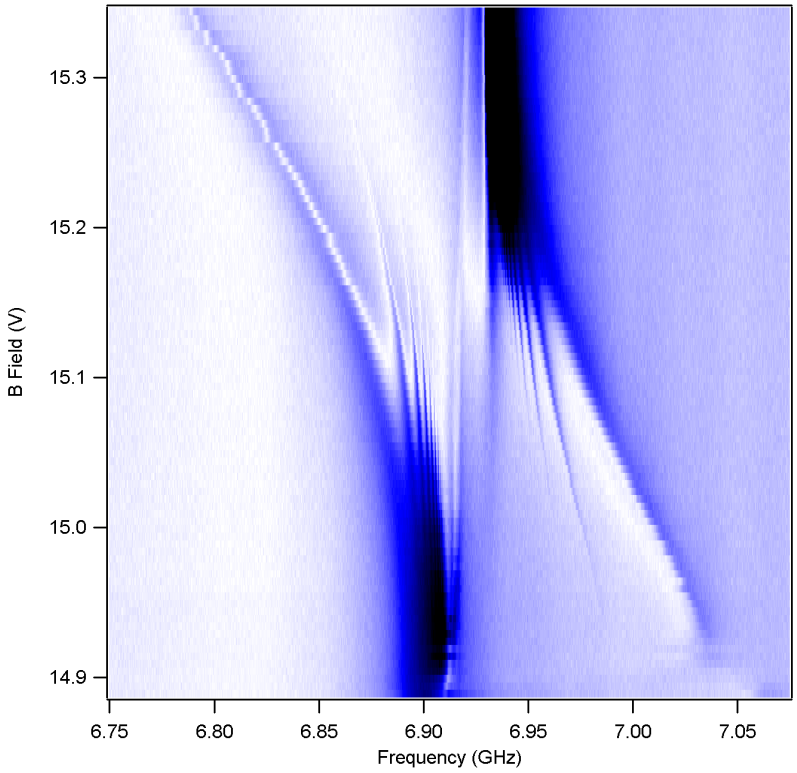

Figure 6.9: The transmon frequency ω_a is controlled by a magnetic field. Colors indicate the transmission of the RF signal at frequency ω_{RF} (blue is high, white is low). RF power is fixed at 4 dBm. Compared to an avoided crossing at low drive power (Fig. 6.1a) additional fan-like structures are visible which arise due to transitions to higher energy levels.

6.4 Measurements at Higher Temperature

In the previous subsection 6.3 thermal peaks were observed between the two Rabi peaks. In order to investigate thermal peaks due to a coupling of the cavity and qubit system to a heat bath, the vacuum Rabi splitting was measured at an elevated temperature of 140 mK. A higher temperature leads to excitations of higher energy levels. A comparison of the plot in Fig. 6.10a with the measurement at a temperature of 20 mK (Fig. 6.7a) shows that two additional peaks at 9 GHz and 9.4 GHz already appear at a drive power of -30 dBm.

The different position in frequency for thermal peaks and peaks obtained with high drive power can be explained with a look at the energy diagram in Fig. 6.10b. A thermal excitation with a subsequent measurement is indicated with solid arrows. The two photon transition leading to the excitation of the same energy level is depicted with dased arrows. There is an energy difference between the high drive power transitions and the measured transition after the thermal excitation, which leads to different positions in frequency.

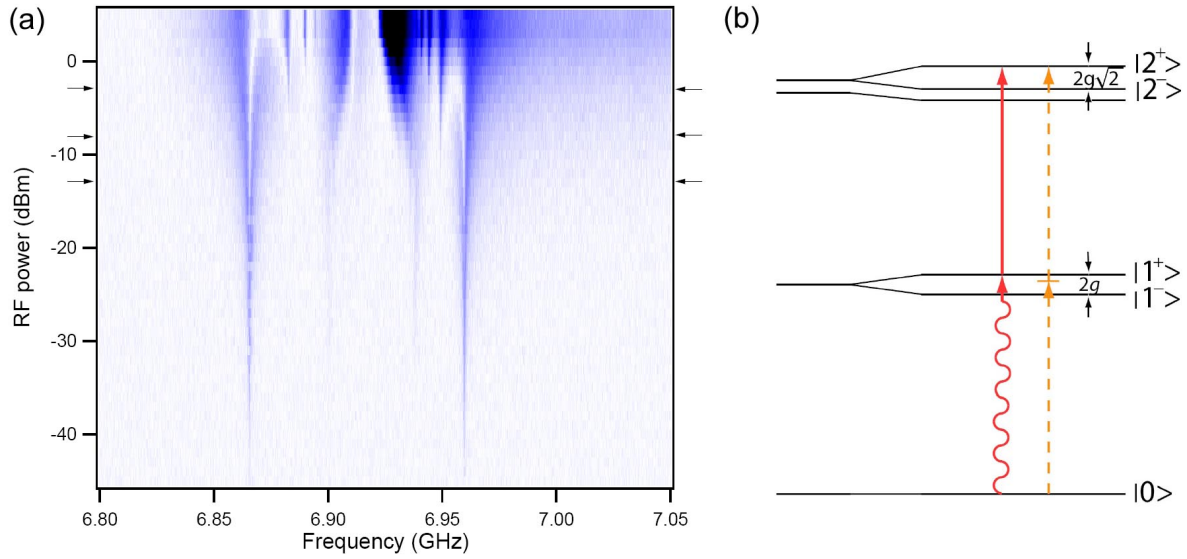

Figure 6.10: (a) Transmission as a function of frequency and RF power. This measurement was executed at a temperature of 120 mK. Already at -30 dBm two additional peaks due to thermal excitations are visible. (b) Energy diagram including two levels. Dashed arrows represent a two photon transition. Solid arrows indicate a thermal excitation from $|0\rangle$ to $|1^+\rangle$ and a subsequent measurement.

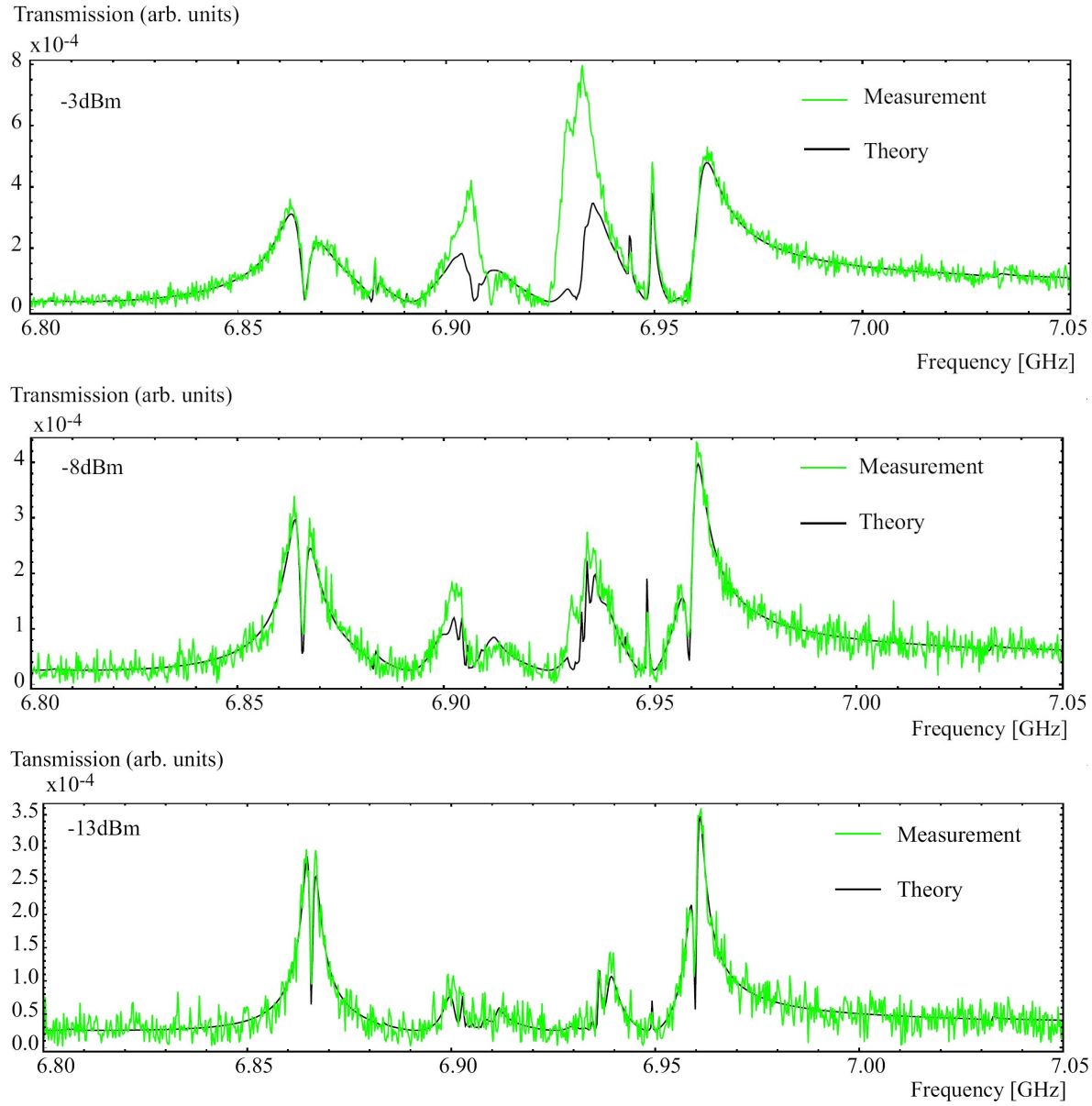

Figure 6.11: Cuts through the plot in Fig. 6.10a at different RF powers (indicated with arrows). For -13 and -8 dBm the simulation is in good agreement with the theory. At higher RF power transitions to higher energy levels become more important and a simulation based on a maximum of seven excitations is no longer accurate. Especially the peaks between 6.9 and 6.94 GHz do not match with the theory.

For the simulation of the system at higher temperature the Lindbladian superoperator in Eq. (2.41) was used. In Fig. 6.11 cuts through the density plot for different powers are shown. For the optimization of the paramters the part from 6.9 GHz to 6.94 GHz was not considered. This restriction can be justified by a look at Fig. 6.12. In this figure the transitions between the energy levels are indicated by lines at the according frequencies. An accumulation of transitions can be observed at frequencies where the two thermal peaks appear. This leads to the conclusion that for a better agreement between measurement and simulation more energy levels should be considered. Unfortunately, we are limited in the number of energy levels for the simulation therefore these datas can not be perfectly explained by the theory. A neglection of the two thermal peaks for the optimization is reasonable.

In Fig. 6.11 a good agreement between simulation and measurement at -13 dBm and -8 dBm is achieved even for the two thermal peaks. At -3 dBm the theory and simulation still coincide except for the intervall from 6.9 GHz to 6.94 GHz. As already mentioned, a maximum of seven excitations are not enough to describe the measurements. From the optimized parameters the thermal prefactor is given by $e^{-\beta\omega}$=0.1. With an average transition frequency of ω=6.9 GHz the temperature of the system can be estimated to 140 mK. The experimentally realized temperature of the cold plate inside the dilution fridge is 120 ± 20 mK.

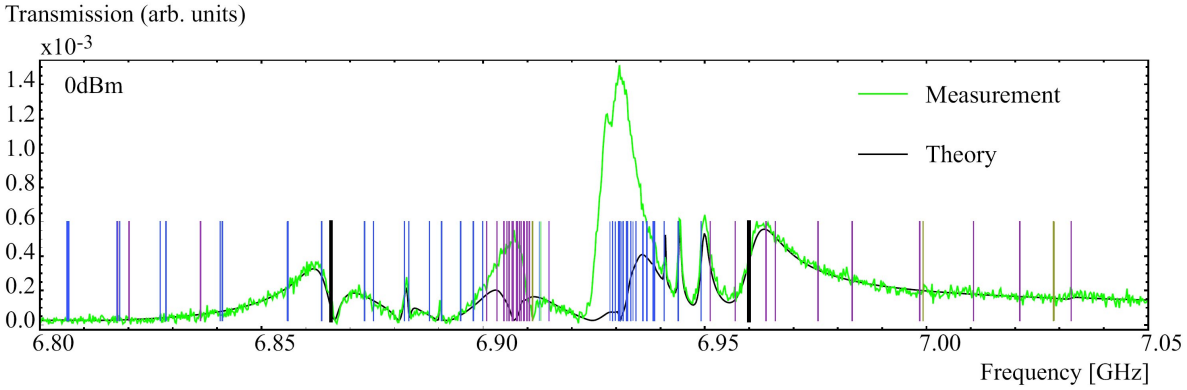

Figure 6.12: Cut through the plot in Fig. 6.10a at 0 dBm RF power. Transitions between energy levels are ploted as lines at the according frequency.

6.4.1 Coupling Strength

According to Eq. (2.14) the coupling strength g increases with $\sqrt{n}$ from the n-1th to the nth energy level. In this idealized case it is assumed that $E_J/E_C \to \infty$. For the measured sample $E_J/E_C = 51$ at resonance and the coupling strength increases not exacly with $\sqrt{n}$. Since the ratio E_J/E_C is rather small for this sample, the exact calculation of the coupling strength could have a significant impact on the transmission.
For a better comparison of $g(E_J/E_C \to \infty)$ and $g(E_J/E_C = 51)$ both cases are plotted for different powers in Fig 6.13. The results show that there is no significant difference visible between the two Lindbladian superoperators and that the system is well described by an idealized $g(E_J/E_C \to \infty)$.

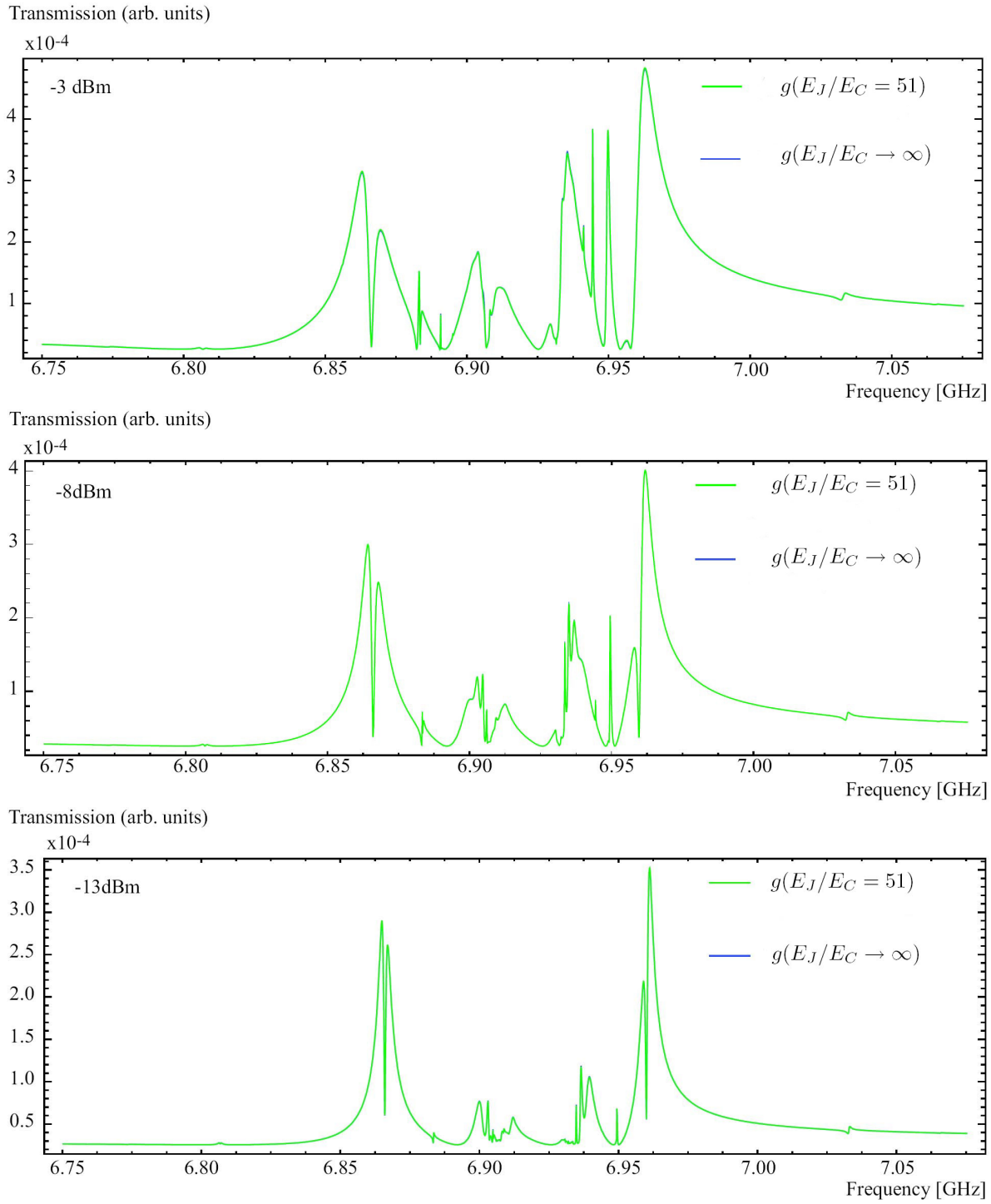

Figure 6.13: Comparison between two different Lindbladian superoperators used for the simulation. In this regime a consideration of the coupling strength dependence of E_J/E_C compared to the idealized case of $g(E_J/E_C \to \infty)$ makes no difference. Due to the smaller step size an additional peak apppears at 6.941 GHz which is not resolved in the simulation plotted in Fig. 6.11.

6.4.2 Dephasing of Higher Energy Levels

All experiments are performed in the transmon regime where charge dispersion is strongly suppressed at least for the lower energy transitions. In terms of charge noise a difference is observable between higher and lower energy levels. Although no sensitivity to n_g is visible for lower energy levels, there is still a charge dispersion remaining for higher energy levels. This leads to the fact that higher energy levels are more affected by charge noise. In our experiment this is the main source for dephasing of the qubit. The different sensitivities of the energy levels to charge noise can be taken into account with a more specified dephasing term in the Lindbladian superoperator.

$$\mathcal{L}[\hat{\rho}_S] = \frac{1}{i\hbar}[\hat{H}, \hat{\rho}_S] + \kappa\mathcal{D}[a]\rho_S + \gamma_1\mathcal{D}[\hat{z}]\rho_S + \frac{\gamma_\phi}{2}\mathcal{D}[\hat{q}']\rho_S \tag{6.10}$$

$$\hat{q}' = \sum_j \{E_j(n_g = 0.5) - E_j(n_g = 0)\} |j\rangle \langle j| \tag{6.11}$$

$\hat{q}'$ represents the total charge dispersion measured from the peak to peak value in the same energy band.

A comparison between data and simulation shows a very good agreement (Fig. 6.14). Especially the two main peaks are fitted well by the simulation. A direct comparison between a Lindbladian superoperator taking into account a higher dephasing at higher energy levels and a Lindbladian superoperator with equal dephasing for every energy level is shown in Fig. 6.15. Differences between the two simulations appear at the top of the two main peaks and for the peak height of the middle section between $6.9 - 6.94$ GHz. The description for the two Rabi peaks is better with faster dephasing for higher energy levels. A reduced peak height is observed in the middle section which is not in agreement with the measurement. Since a least square optimization between data and theory is done discarding the middle part between 6.9 GHz and 6.94 GHz this should not be taken into account.

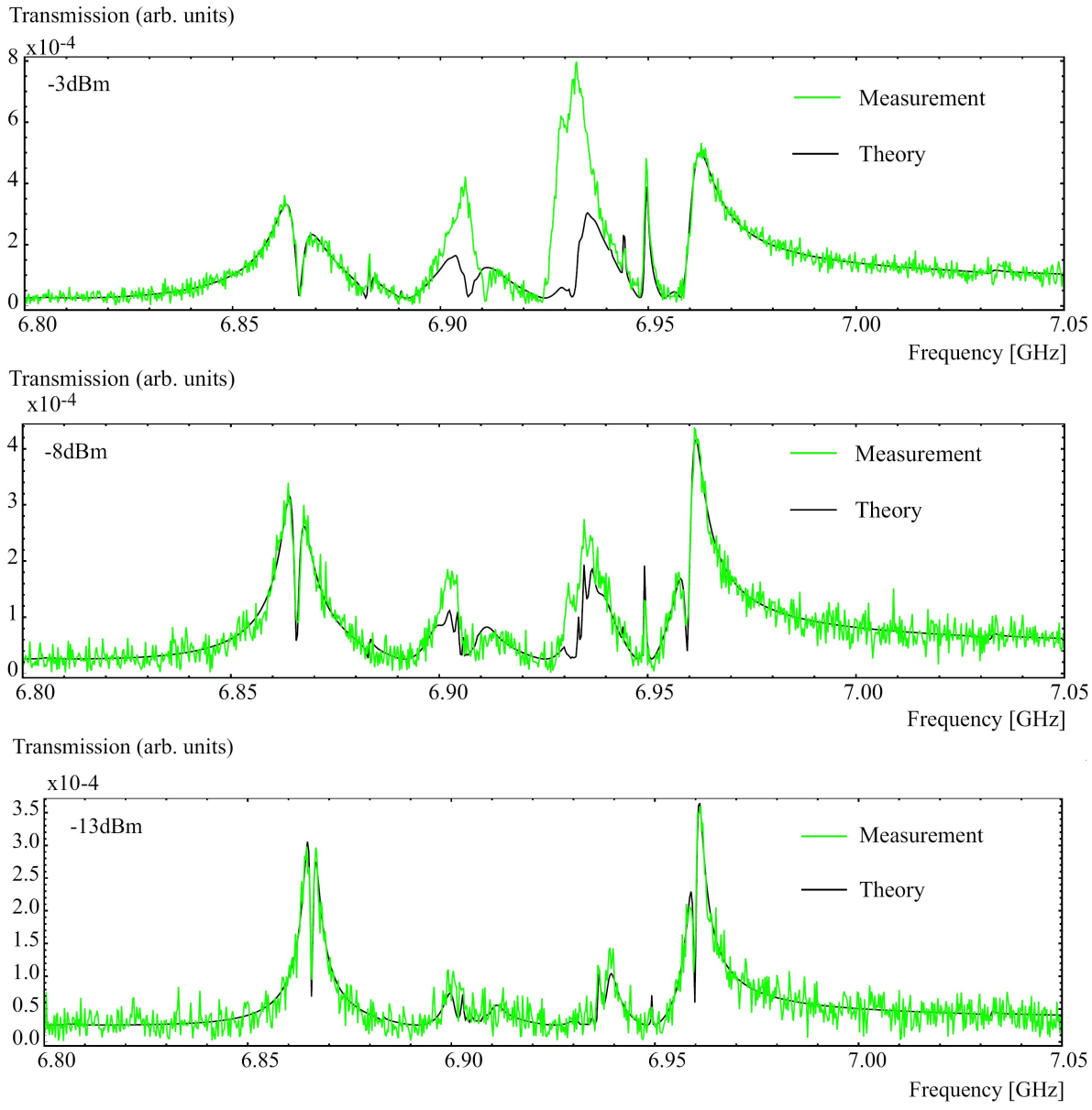

Figure 6.14: Measurement and corresponding simulation based on the Lindbladian superoperator in Eq. (6.11), which takes an increased dephasing for higher energy levels into account.

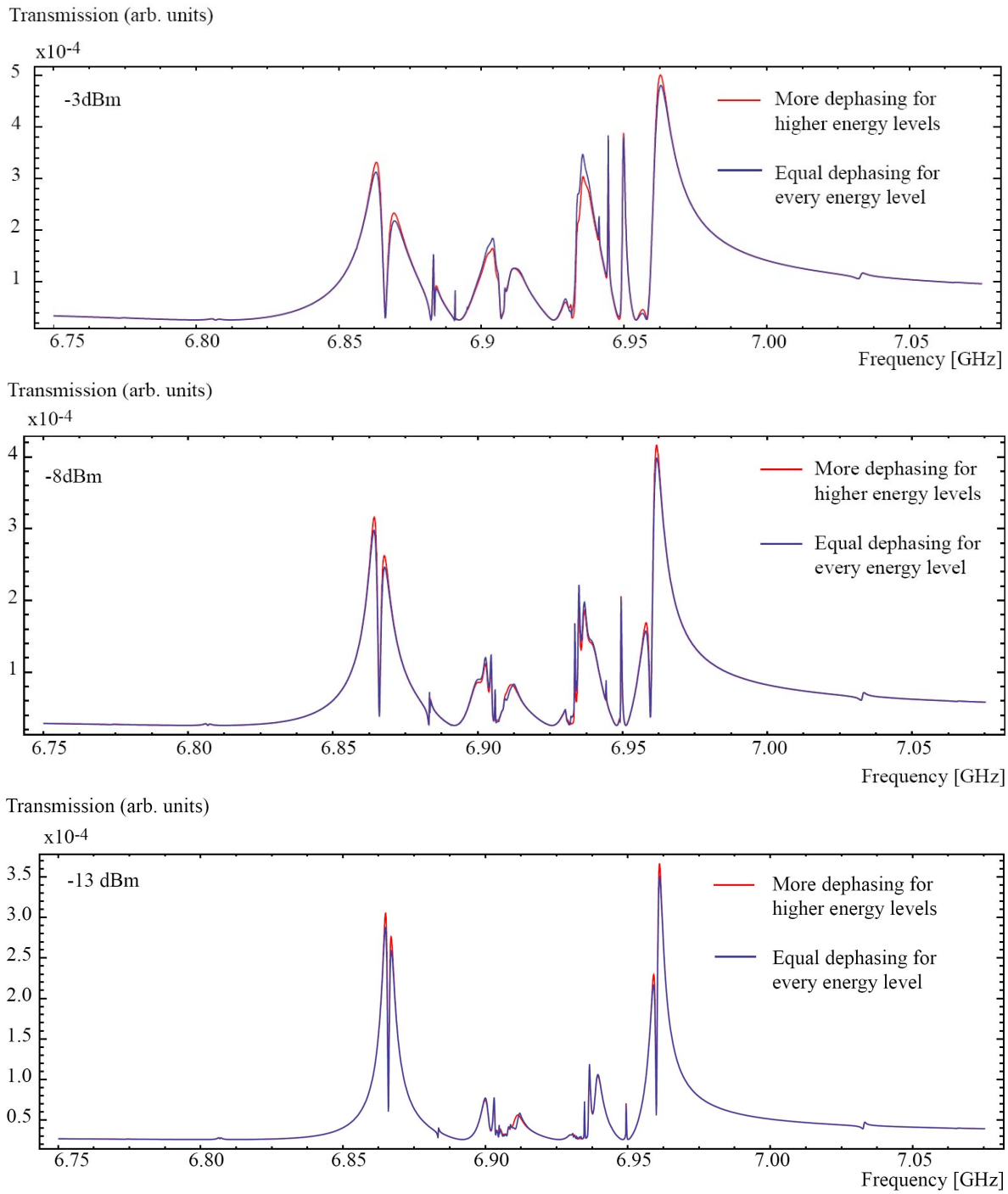

Figure 6.15: Comparison between a simulation with higher γ_ϕ for higher energy levels and a simulation that has the same dephasing for every energy level. A difference in the height of the two Rabi peaks is visible. With higher γ_ϕ for higher energy levels a better agreement between theory and measurement for the two Rabi peaks is reached. An additional peak is visible compared to Fig. 6.14 because of the smaller step size in frequency.

6.4.3 Avoided Crossing at High Drive Power

The main differences between the avoided crossing at high temperature (Fig. 6.16) and at low temperature (Fig. 6.9) are an increased transmission at the resonator frequency $\omega_r = 6.92$ GHz and two lines with decreased transmission at a magnetic field of 15.03 V and 15.16 V, respectively.
For a better understanding of the measurement the avoided crossing was simulated with a maximum number of six excitations (Fig. 6.17b). For this simulation optimized parameters over different powers were used and the dependence of E_J on the magnetic field was determined experimentally. There are two evident differences between experiment and simulation, the two lines with decreased transmission for 15.05 V and 15.16 V disappeared and the transmission peaks at the cavity resonance frequency are further separated form each other. As already mentioned in Chapter 4, two qubits are placed on the measured sample. The presence of the second qubit influences the measured qubit. Since the simulations take only one qubit into account, this could be a reason for the difference between measurement and simulation.

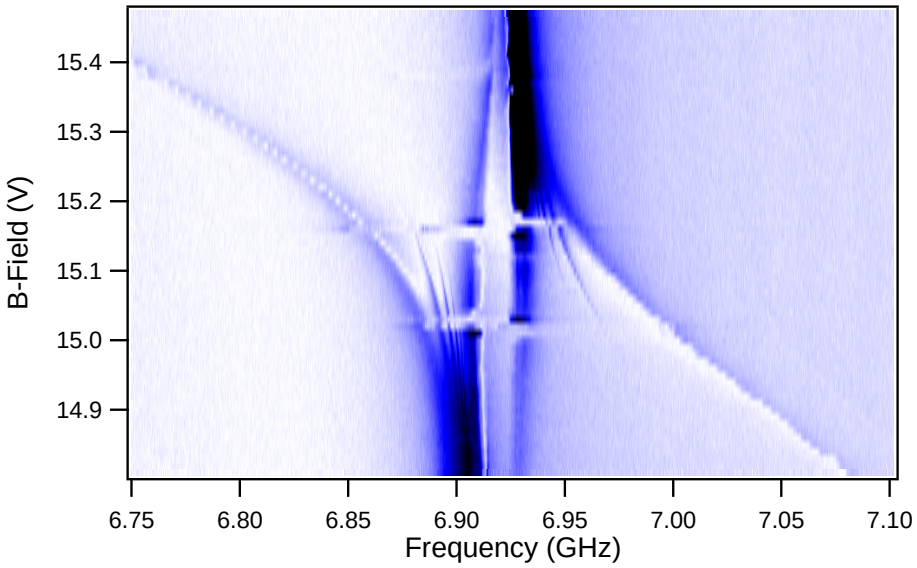

Figure 6.16: The transmon frequency ω_a is tuned by a magnetic field. Colors indicate transmission of the RF signal at frequency ω_{RF} (blue is high, white is low). The temperature is set to 140 mK and RF power is fixed at -1 dBm.

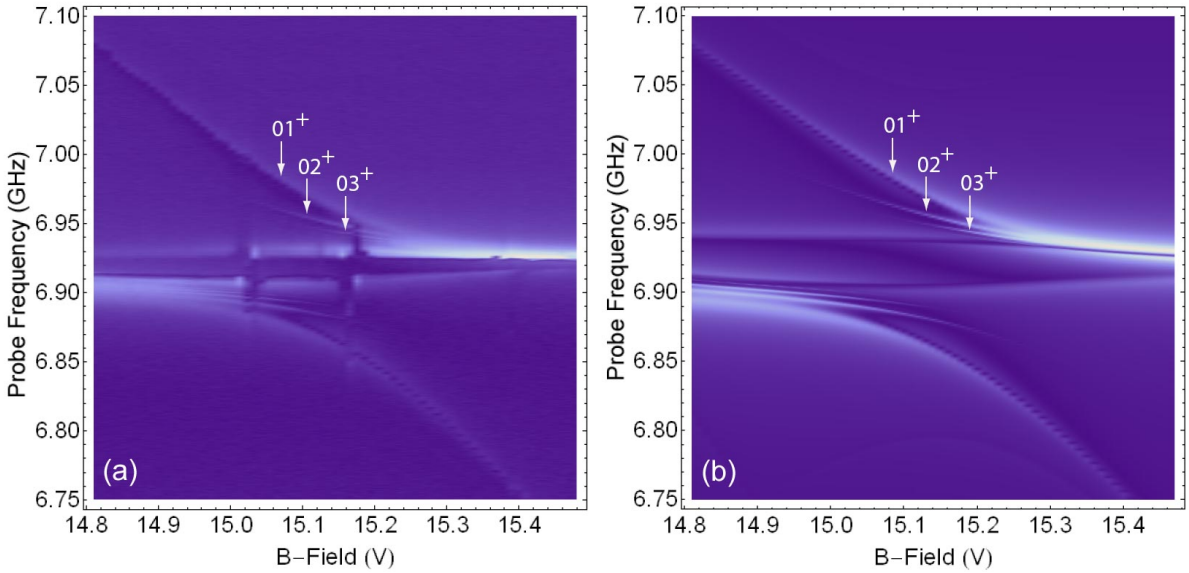

Figure 6.17: (a) Measurement for an avoided crossing at a temperature of 140 mK and RF power of -1 dBm. High transmission is colored white and low transmission dark blue. (b) Simulation of the avoided crossing. Two lines with decreased transmission at 15.03 V and 15.16 V respectively, are not visible in the simulation, they appear most likely due to the presence of a second qubit on the same chip. The transmission peaks close to the cavity resonance frequency are further separated form each other compared to the measurement. This separation is due to the limited number of levels in the simulation. A consideration of more energy levels would lead to a frequency shift for the thermal peaks (Fig. 6.12).

6.5 Determination of Thermal Photon Numbers

In the previous section good agreement between measurement and simulation at increased temperature up to 140 mK was observed for sufficiently small coherent drive strengths. If the measurements are performed in this range and all relevant sample parameters are well known, it is interesting to try to use the measurement of the Vacuum Rabi splitting as a 'thermometer' for the effective cavity and qubit system.

The sample is placed on the cold plate inside the resonator. A more convenient way to determine the temperature of the effective cavity and qubit system compared to the vacuum Rabi splitting measurement would be to measure the cold plate temperature. The main problem of this method is that thermal photons from the drive lines heat up the sample, which leads to a temperature gradient between the cold plate and the sample.

6.5.1 Simulation of Thermal Noise

An increase of the real temperature with the dilution fridge can not be realized as accurate as needed and leads to unwanted changes in the sample like the loss of superconductivity for a temperature higher than T_c. Therefore an other approach was chosen where only the electromagnetic signal that enters the cavity is at an increased temperature. To simulate thermal noise that would arise in an electromagnetic field at increased temperature, noise is added to the resonator input.

White noise is created with an arbitrary wave form generator (AWG) outside of the dilution fridge. The frequency bandwidth of the noise is limited to 0.4 GHz due to the AWG bandwidth. Therefore the noise must be centered to the resonator frequency with a mixer. The noise signal must be amplified before it enters the mixer, to ensure that the leakage signal of the mixer vanishes inside the noise signal. To tune the noise power, a variable attenuator is used. Finally the noise signal is combined together with the RF signal and enters the dilution fridge on the same line. In order to change the temperature of the signal, different noise powers are applied to the resonator input (Fig. 6.19).

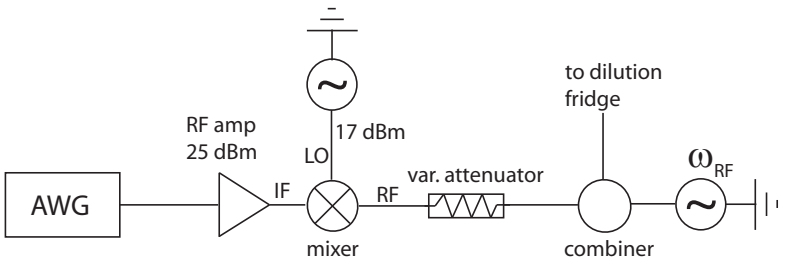

Figure 6.18: Experimental setup for the simulation of thermal noise.

In experiments presented in the previous section 6.4 the sample was physically heated which led to an occupation of higher qubit modes and higher cavity modes under the assumption of a

thermal equilibrium between cavity and qubit system. With this assumption a good agreement between theory and measurement was reached.
For experiments in this section only the signal is at an increased temperature. A drive signal with additional thermal noise yields an occupation of higher cavity modes. Since the anharmonicity of the transmon qubit is low, again higher qubit levels will be occupied and are relevant for the simulation. Therefore a theoretical description with the same model is reasonable.

6.5.2 Photon Number and Power Spectral Density

The average photon number of a thermal electromagnetic field is given by [37]

$$\bar{n} = \frac{1}{e^{\frac{\hbar\omega}{k_B T}} - 1}. \tag{6.12}$$

The spectral density of power for a one dimensional electromagnetic field can be described by the one dimensional black body radiation spectrum

$$S(\omega) = \frac{\hbar\omega}{e^{\frac{\hbar\omega}{k_B T}} - 1}. \tag{6.13}$$

The spectral density of power is plotted versus frequency in Fig. 6.19. As already mentioned in section 6.5.1 noise with a constant spectral density of power is applied to the resonator input. This approximation is only valid for high temperatures since $S(\omega)$ decreases exponentially in frequency for low temperatures (Fig. 6.19).

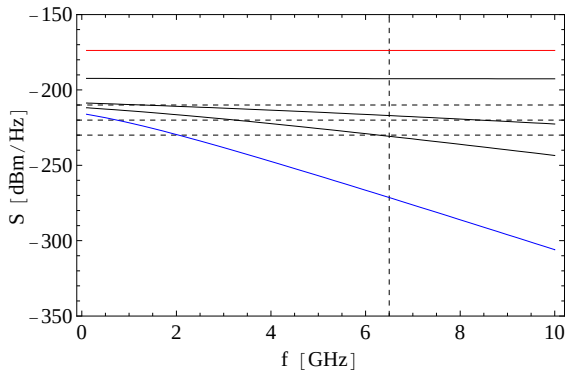

Figure 6.19: Spectral density of power at temperatures 300 K, 4 K, 100 mK, 50 mK and 20 mK from top to bottom. Dashed lines represent the spectral density at a frequency of 6.5 GHz on the resonator input with photon numbers of n=0.1, 0.01, 0.001. Figure taken from [38].

According to reference [38], the general case in Eq. (6.13) can be specialized to the relevant noise spectrum which is that of a 50 Ω matched attenuator on the transmission lines connecting from room temperature to 20 mK. This leads to a geometric prefactor of $\pi/8$. With a constant

offset n_0 that takes finite temperature into account, the photon number inside the cavity is given by

$$n = \frac{\pi}{8} \cdot \frac{S(\omega)}{\hbar\omega} + n_0. \tag{6.14}$$

From equation (6.14), the extracted photon number from the simulation is expected to be linear with the applied noise power spectrum. The offset n_0 leads to a temperature of the cavity and qubit system. By observing this temperature it can be judged whether the thermal noise on the coupled lines is low enough to prevent a thermal population of higher energy levels.

6.5.3 Measurements

All measurements in this section are performed at ETH Zurich with a sample with the following parameters are slightly. The qubit has a charging energy of $E_C/h = 231.7$ MHz and a maximum Josephson energy of $E_J^{max}/h = 35.11$ GHz, the coupling constant is given by $g/\pi = 265$ MHz. The cavity can be characterized with a resonant frequency of $\omega_r/2\pi = 6.440$ GHz and a width of $\kappa/2\pi = 1.57$ MHz.

In Fig. 6.20 the vacuum Rabi Splitting is shown for three different noise powers with a constant drive power of -30 dBm. Increased noise powers were taken into account with a higher temperature parameter in the simulation, all other parameters were fixed. The simulation is in good agreement with the measurement, especially for the thermal peaks that are enlarged in an inset. For this sample the coupling constant g was higher and therefore the Rabi peaks were seperated to a larger extent than in previously measured vacuum Rabi splittings.

Thermal peaks in the vacuum Rabi splitting with increasing noise power from bottom to top are shown in Fig. 6.21a. To get a good fit to the data, a nonlinear least square optimization was performed on the temperature parameter from 6.455 to 6.555 GHz. For low noise power the simulation is a good description of the measurement. At higher noise power the height of the two thermal peaks is not well fitted.

The average photon numbers can be extracted from the simulation and are plotted as a function of the power spectral density in Fig. 6.21b. The absolute value of the applied power spectral density was obtained with an ac Stark shift measurement [39]. A linear fit to the measurement points is indicated with a red line. As expected, a linear dependence of the thermal photons to the power spectral density can be observed. However, the slope does not match with the theoretical prediction of a $\pi/8$ geometrical prefactor. Further investigations are needed to understand this discrepancy.
The offset of 90 mK arises due to real thermal excitation of the signal which can be caused by too little attenuation or not well enough thermalized attenuators. In a next step the signal temperature should be decreased to prevent thermal population of higher energy levels and to ensure that the cavity is in the ground state.

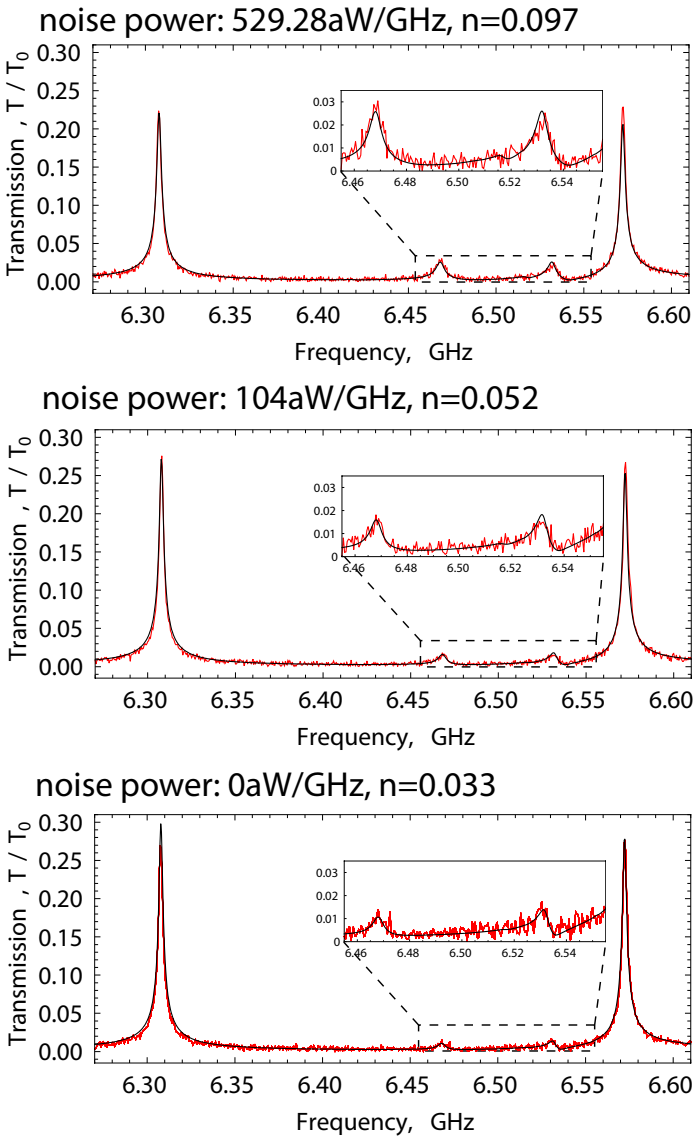

Figure 6.20: Vacuum Rabi mode splitting for three different noise powers measured with a coherent drive power of -30 dBm. The simulation is in good agreement with the measurement, especially for the thermal peaks which are enlarged in an inset. The parameters of the simulation are $\omega_r = 6.4365$GHz, $\delta = -7$ MHz, $2g = 264.3$ MHz, $\gamma_\phi = 0.9$ MHz, $E_J/E_C(\omega_r) = 112.211$, $\gamma_1 = 1.9$ MHz, $\frac{\kappa}{2\pi} = 1.57$ MHz, $\alpha = 9.8206 \cdot 10^{-6}$,$b = 7\ \mu$V, $pt = -62$, $pt_\phi = -5$, $\xi = 10^{128.44/20}$ Hz.

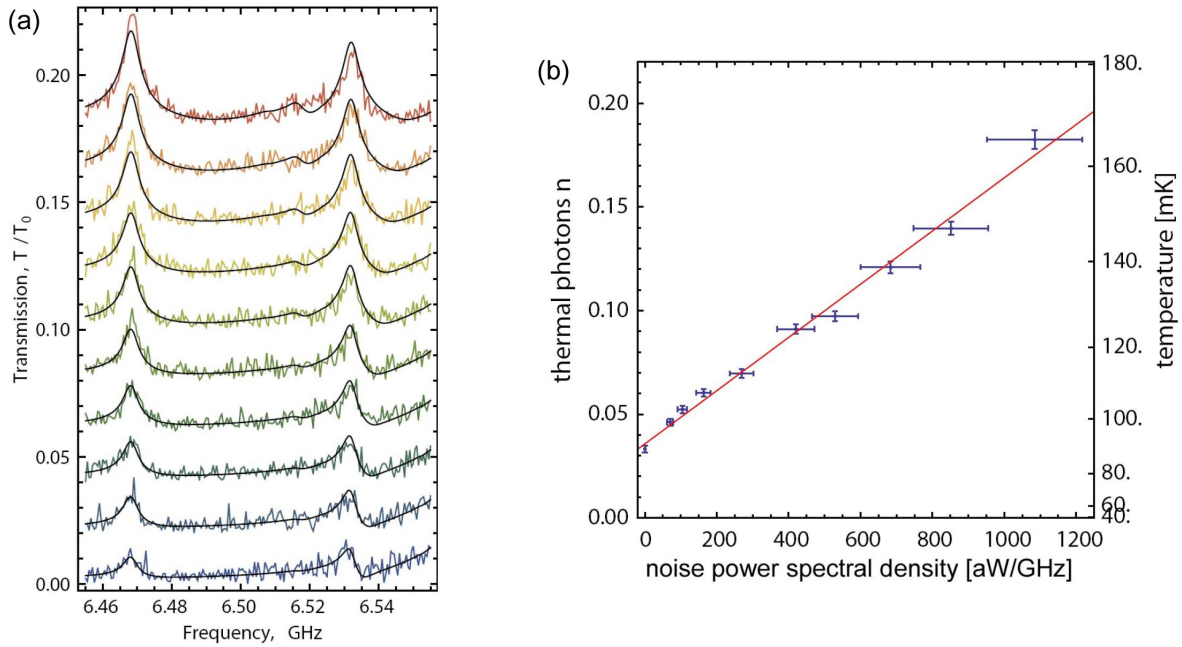

Figure 6.21: (a) Thermal peaks in the vacuum Rabi splitting plotted from bottom to top with increasing noise power. An offset of 0.02 T/T_0 was generated between the curves for a better visibility. For low noise power the simulation is a good description of the measurement. At higher noise power the height of the thermal peaks is not well fitted. (b) The average thermal photon number and the temperature extracted from the simulated thermal peaks is plotted as a function of the noise power. The red line is a linear fit to the measurement points.

Chapter 7

Conclusion

The observation of the vacuum Rabi splitting for high probe powers led to additional features in the transmission spectrum. At high RF powers the Rabi peaks change their shape from Lorentzian to a doublet and additional peaks appear in the spectrum due to multi-photon transitions to higher energy levels.

In order to explain the observed Rabi peak splitting the transmon and cavity system was approximated by its lowest two levels. An intuitive picture with the quasi spin rotating around an effective B-field gives a better understanding for a dip in the Rabi peak. With a more analytical model given by Bloch equations a description of the Rabi peak splitting over different powers is possible. The asymmetry of the peaks in the measurement is due to transitions to higher energy levels. A good agreement with the measurement was reached with a numerical calculation that takes a maximum number of seven excitations into account. This simulation was written in Mathematica and calculates the transmon levels in charge basis. For a description of the entire system the master equation was solved in steady state.
Not only for the description of the Rabi peak supersplitting was this simulation useful. Especially the peaks that arise due to transitions to higher energy levels could be described really well. For the measurement at 140 mK a temperature dependent coupling to the environment was considered in the master equation. This led to good agreement with experimental data in the low power regime. A description at higher temperature would need to take more energy levels into account. An adoption of the program to include more energy levels would require an optimization of the algorithm to keep the calculation time within reasonable limits.
At low drive power and temperature the simulation of the vacuum Rabi mode splitting spectrum was used as a measurement of the effective cavity and qubit system temperature. In order to change the temperature, noise with different power spectral densities was added to the resonator input. As theoretically predicted, a linear increase of the thermal photon number with noise power spectral density was observed. An offset of 90 mK corresponding to a thermal intra-cavity photon number could be determined very accurately.

With the agreement between measurement and simulation in every peak, the theoretical description of the system by a generalized Jaynes-Cummings Hamiltonian and its $\sqrt{n}$ nonlinearity is confirmed. Another approach could be a more accurate consideration of the sample temperature with two different heat baths: one for the cavity modes and one for the qubit modes.

Further investigations are needed to understand the slope of thermal photons as a function of noise power spectral density more accurately. In a next step the temperature of the cavity and qubit system should be decreased with more attenuation or a better thermalization of the attenuators to avoid unwanted thermal population of qubit levels and to ensure that the cavity is in the ground state.

Appendix A

Acknowledgements

First of all, I would like to thank Prof. Andreas Wallraff for giving me the possiblity to work on this fascinating topic. He made it possible for me to do a part of the diploma thesis at Yale University and I want to express my gratitude for his support and encouragement.

I would especially like to thank Prof. Schoelkopf for giving me the opportunity to work in his group. I also want to thank Jerry Chow, who showed me the experimental part of cavity QED with a lot of ethusiasm and patience. A big thank goes to Lev Bishop. He introduced a fascinating theoretical description of cavity QED to me and supported me with his Mathematica knowledge. I enjoyed the motivating spirit of the whole Schoelkopf group and would like to thank everybody for discussing physical and non-physical topics.

Another thank goes to my colleagues at the Quantum Device Lab. Always was somebody there if an advice or a helping hand was needed. I would especially like to thank Johannes Fink with whom I worked together on the thermal photon project. Furthermore, Stefan Filipp is aknowledged for sparing no effort answering my questions.

Finally I would like to thank my family for supporting me during the years of my studies.

Bibliography

[1] J. M. Raimond, M. Brune, S. Haroche, *Manipulating quantum entanglement with atoms and photons in a cavity*, Rev. mod. Phys. **73**, 565 (2001).

[2] J. P. Reithmaier, G. Sek, A. Loffler, C. Hofmann, S. Kuhn, S. Reitzenstein, L. V. Keldysh, V. D. Kulakovskii, T. L. Reinecke, A. Forchel, *Strong coupling in a single quantum dot – semiconductor microcavity system*, Nature **432**, 197-200 (2004).

[3] A. Wallraff, D. I. Schuster, A. Blais, L. Frunzio, R.-S. Huang, J. Majer, S. Kumar, S. M. Girvin and R. J. Schoelkopf, *Strong coupling of a single photon to a superconducting qubit using circuit quantum electrodynamics*, Nature **431**, 162 (2004) (reprint).

[4] P. W. Shor, *Polynomial − time algorithms for prime factorization and discrete logarithms on a quantum computer*, Siam J. Sci. Statist. Comput. **26**, 1484 (1997)

[5] R. L. Rivest, A. Shamir, L. Adleman, *A method for obtaining digital signatures and public − key cryptosystems*, Commun. ACM **21**, 120-126 (1978).

[6] L. K. Grover. *Quantum mechanics helps in searching for a needle in a haystack*, Phys. Rev. Lett. **79**, 325-328 (1997).

[7] S. Lloyd, *Quantum Information Matters*, Science **319**, 1209-1211 (2008).

[8] R. P. Feynman, *Simulating physics with computers*, International Journal Of Theoretical Physics 21, 467-488 (1982).

[9] D. P. DiVincenzo, *The physical implementation of quantum computation*, Fortschritte der Physik **48**(9-11):771-783, (2000).

[10] J. Koch, T. M. Yu, J. Gambetta, A. A. Houck, D. I. Schuster, J. Majer, A. Blais, M. H. Devoret, S. M. Girvin, R. J. Schoelkopf, *Charge insensitive qubit design derived from the Cooper pair box*, Phys. Rev. A76, 042319 (2007).

[11] A. Furusawa, J. L. Sørensen, S. L. Braunstein, C. A. Fuchs, H. J. Kimble, E. S. Polzik, *Unconditional Quatnum Teleportation*, Science **282**(5389): 706 - 709 (1998)

[12] Y. Zhu, D. J. Gauthier, W. E. Morin, Q. Wu, H. J. Carmichael, T. W. Mossberg, Vacuum Rabi Splitting as a Feature of Linear-Disperion Theory: Analysis and Experimental Observations, Phys. Rev. Lett. 64, 2499-2502(1990).

[13] A. Blais, R.-S. Huang, A. Wallraff, S. M. Girvin, R. J. Schoelkopf, *Cavity quantum electrodynamics for superconducting electrical circuits : An architecture for quantum computation.* Phys. Rev. A 69, 062320 (2004).

[14] D. I. Schuster, *Circuit Quantum Electrodynamics*, Dissertation, Yale University, 2007.

[15] J. A. Schreier, A. A. Houck, J. Koch, D. I. Schuster, B. R. Johnson, J. M. Chow, J. M. Gambetta, J. Majer, L. Frunzio, M. H. Devoret, S. M. Girvin, R. J. Schoelkopf, *Suppressing Charge Noise Decoherence in Superconducting Charge Qubits*, arXiv:0712.3581v1 (2007).

[16] J. Clarke, F. K. Wilhelm, *Superconducting quantum bits*, Nature **453**, 1031-1042 (2008)

[17] R. J. Schoelkopf, S. M. Girvin, *Wiring up quantum systems*, Nature **451**, 7179 (2008), pp. 664-669.

[18] V. Bouchiat, D. Vion, P. Joyez, D. Esteve, M. H. Devoret, *Quantum Coherence with a Single Cooper Pair*, Physica Scripta Vol. T76, 165-170 (1998).

[19] M. Tinkham, *Introduction to Superconductivity.* McGraw-Hill International Editions, (1996).

[20] D. Vion, A. Aassime, A. Cottet, P. Joyez, H. Pothier, C. Urbina, D. Esteve, M. H. Devoret, *Manipulating the Quantum State of an Electrical Circuit*, Science **296**(5569): 886 - 889 (2002).

[21] J. M. Fink, M. Goeppl, M. Baur, R. Bianchetti, P. J. Leek, A. Blais, A. Wallraff, *Climbing the Jaynes−Cummings Ladder and Observing its $\sqrt{n}$ Nonlinearity*, Nature **454**, 315-318 (2008).

[22] A. Cottet, *Implementation of a quantum bit in a superconducting circuit*, Dissertation, CEA Saclay, France, 2002.

[23] M. Goeppl, A. Fragner, M. Baur, R. Bianchetti, S. Filipp, J. M. Fink, P. J. Leek, G. Puebla, L. Steffen, A. Wallraff, *Coplanar Waveguide Resonators for Circuit Quantum Electrodynamics*, arXiv:0807.4094v1 (2008).

[24] L. Frunzio, A. Wallraff, D. Schuster, J. Majer, R. Schoelkopf, *Fabrication and Characterization of Superconducting Circuit QED Devices for Quantum Computation*, IEEE transactions on applied superconductivity, Vol. 15, No. 2 (2005).

[25] D. Pozar, *Microwave engineering.* Addison-Wesley Publishing Company (1993).

[26] A. Wallraff, J. Majer, L. Frunzio, R. J. Schoelkopf, *Superconducting solid state cavity QED : Notes on resonators*, 2003.

[27] A. Blais, J. Gambetta, A. Wallraff, D. I. Schuster, S. M. Girvin, M. H. Devoret, R. J. Schoelkopf Physical Review A 75(3), 032329 (2007).

[28] L. S. Bishop, J. Koch, *Rotating Wave Approximation and Rotating Frame*, private communications.

[29] G. J. Dolan, *Offset masks for lift-off processing* , Appl. Phys. Lett. **31**, 337-339 (1977).

[30] R. N. Simons, *Coplanar waveguide circuits, components and systems*. Wiley Series in Microwave and Optical Engeneering, Wiley Inter-Science (2001).

[31] S. Haroche, J. M. Raimond, *Exploring the Quantum, Atoms, Cavities and Photons*. Oxford University Press Inc., New York (2006).

[32] R. Alicki, K. Lendi, *Quantum Dynamical Semigroups and Applications*. Lect. Notes in Phys. 171, Springer, Berlin Heidelberg (2007).

[33] J. Majer, J. M. Chow, J. M. Gambetta, Jens Koch, B. R. Johnson, J. A. Schreier, L. Frunzio, D. I. Schuster, A. A. Houck, A. Wallraff, A. Blais, M. H. Devoret, S. M. Girvin, R. J. Schoelkopf, *Coupling Superconducting Qubits via a Cavity Bus*, arXiv:0709.2135v1 (2007).

[34] D. W. Marquardt, *An Algorithm for Least-Squares Estimation of Nonlinear Parameters*, Journal of the Society for Industrial and Applied Mathematics, Vol. 11, No. 2 (1963), pp. 431-441.

[35] J. Dalibard, J.-M. Raimond, J. Zinn-Justin, *Systmes fondamentaux en optique quantique*,Ecole d'été de physique théorique No53, Les Houches , FRANCE (25/06/1990).

[36] J. M. Fink, *Single Qubit Control and Observation of Berry's Phase in a Superconducting Quantum Circuit*. Master thesis, Universität Wien, 2007.

[37] D. Walls and G. Milburn, *Quantum Optics*. Springer, 1st ed. 1994. 2nd printing edition, February (2005).

[38] P. Leek, *Thermal noise & resonators...*, 2008.

[39] D. I. Schuster, A. Wallraff, A. Blais, L. Frunzio, R.-S. Huang, J. Majer, S. M. Girvin, R. J. Schoelkopf, *ac Stark Shift and Dephasing of a Superconducting Qubit Strongly Coupled to a Cavity Field*, PRL **94**, 123602 (2005).